INVESTIGATING THE PETROGENESIS OF THE NAIFEH AND PLUMERIA SEAMOUNTS: INSIGHTS INTO THE GEOCHEMICAL DIVERSITY OF SEAMOUNTS ADJACENT TO THE HAWAIIAN SEAMOUNT CHAIN

by

Geoffrey Montour

A thesis

submitted in partial fulfillment

of the requirements for the degree of

Master of Science in Geosciences

Boise State University

May 2023

BOISE STATE UNIVERSITY GRADUATE COLLEGE

DEFENSE COMMITTEE AND FINAL READING APPROVALS

of the thesis submitted by

Geoffrey Montour

Thesis Title: Investigating the Petrogenesis of the Naifeh and Plumeria Seamounts: Insights into the Geochemical Diversity of Seamounts Adjacent to the Hawaiian Seamount Chain

Date of Final Oral Examination: 07 December 2022

The following individuals read and discussed the thesis submitted by student Geoffrey Montour, and they evaluated the student's presentation and response to questions during the final oral examination. They found that the student passed the final oral examination.

Dorsey Wanless, Ph.D.	Chair, Supervisory Committee
Mark Schmitz, Ph.D.	Member, Supervisory Committee
Darin Schwartz, Ph.D.	Member, Supervisory Committee

The final reading approval of the thesis was granted by Dorsey Wanless, Ph.D., Chair of the Supervisory Committee. The thesis was approved by the Graduate College.

ACKNOWLEDGMENTS

This research could not have been completed without the support of my advisor Dorsey Wanless, her encouragement and feedback were invaluable throughout this process. I'd like to thank my committee, Mark Schmitz and Darin Schwartz for their knowledge and expertise. I would also like to express my deepest appreciation to my friends and family for their support and motivation. Finally, many thanks to the 2018 crew of E/V Nautilus for collecting the lavas used in this thesis.

ABSTRACT

The Naifeh and Plumeria seamount clusters, which consist of 10 submarine volcanoes located ~220km north of the Northwest Hawaiian Ridge, were mapped and sampled by the E/V Nautilus expedition NA101 in 2018. The origin of these seamounts is unknown, but their unique orientation and location imply several possible mechanisms of formation. Four possible mechanisms of formation include: 1) off-axis upwelling of the Hawaiian mantle plume, 2) ancient arch volcanism, 3) intraplate extension and deformation, 4) hotspot volcanism. Investigating the origin of these seamount clusters will better constrain the composition of the underlying mantle, as well as the depth and extent of melting required to generate these large volcanic structures and provide insight into the interaction between mantle plumes, the upper mantle, and surrounding lithosphere.

Here we present major and trace element compositions of 28 samples from the five Naifeh seamounts and 22 samples from the five Plumeria seamounts. Major element data indicate that all lavas are alkalic, ranging from trachybasalts to trachyandesites. The lavas from both seamount chains have low MgO contents (0.62-2.31 wt.%) and are cogenetic. Trace element patterns are relatively consistent throughout both chains, suggesting the lavas came from a similar mantle source and extent of partial melting. Naifeh and Plumeria both have enriched incompatible trace element compositions compared to mid ocean ridge basalts (MORB), suggesting their source is not typical

depleted upper mantle, but more similar to a mixture of ocean island basalt (OIB) and enriched-mid ocean ridge basalt (EMORB), and normal MORB. Thus, it is not likely these were formed simply from intraplate extension and deformation as has been suggested for the nearby Musician seamounts or from Cretaceous crust building. The seamounts are also distinct from North and South Arch lavas, suggesting that they were not created from melting beneath the flexural bulge associated with plate loading. Instead, Naifeh and Plumeria have compositions similar to lavas from the Line Islands and Rurutu, which have been explained by multiple hotspots stemming from the South Pacific Superswell or small scale sublithospheric convection. Naifeh and Plumeria also have compositional similarities with the Shatsky, Ojin, and Hess rise seamounts, which are hotspot derived seamounts erupted during the early to mid-Cretaceous. Based on this, we suggest that the Naifeh and Plumeria seamounts originated from a hotspot source emanating from the South Pacific Superswell with the incorporation of recycled oceanic crust or are a product of small scale sublithospheric convection.

TABLE OF CONTENTS

LIST OF TABLES

LIST OF FIGURES

LIST OF PICTURES

LIST OF ABBREVIATIONS

BSU	Boise State University
MORB	Mid Ocean Ridge Basalt
N-MORB	Normal Mid Ocean Ridge Basalt
E-MORB	Enriched Mid Ocean Ridge Basalt
REE	Rare Earth Element
HREE	Heavy Rare Earth Element
LREE	Light Rare Earth Element
ROV	Remote Operated Vehicle
E/V	Exploration Vessel
SOPITA	South Pacific Isotopic and Thermal Anomaly
ICP-MS	Inductively Coupled Plasma Mass Spectrometer
XRF	X-ray Fluorescence
BTA	Basaltic Trachyandesite
TA	Trachyandesite
TB	Trachybasalt
SSC	Small-scale Sublithospheric Convection

INTRODUCTION

Seamounts are isolated topographic features, typically volcanic, that stand greater than 100 m above the surrounding seafloor (Staudigel and Clague, 2010). The oceanic crust is littered with seamounts, with some estimates suggesting >30,000 seamounts in the Pacific alone (Wessel et al., 2010). Despite their abundance, less than 0.1% have been directly observed or sampled, and the origin of most seamounts have not been investigated (Staudigel and Clague, 2010). Due to their remote nature, most of our knowledge of seamounts comes from satellite observations of seafloor topography (Staudigel and Clague, 2010). Seamounts vary in morphology, forming linear chains, small clusters, or individual cones. Flat topped seamounts are commonly defined as "guyots" and are likely to have once been islands, while conical seamounts have likely never breached the sea surface (Staudigel and Clague, 2010). Seamounts/guyots are not only diverse in their morphology, but can vary in composition as well, which has been attributed to various degrees of melting of a heterogeneous mantle or variations in shallow magmatic processes (Winter, 2010). The lack of sampling and direct observation makes it difficult to answer fundamental questions on the origin of these abundant volcanic structures.

The goal of this study is to investigate the petrogenesis of lavas erupted at two previously unexplored seamount clusters (Naifeh and Plumeria); located ~220 km north of the Gardner and Necker seamounts of the Hawaiian-Emperor seamount chain (Figure 1 & 2). The origin of these two seamount clusters is intriguing because they are aligned

roughly parallel to the Hawaiian-Emperor Seamount Chain, are located at the end of a long fracture zone, and are situated on top of the Hawaiian Arch, which is a broad swell in the lithosphere surrounding the Hawaiian-Emperor chain (Lipman et al. 1989; Frey et al., 2000). However, they also lie among the thousands of other seamounts that sit on the Pacific seafloor that have no obvious origin. This location and geometry results in several possible hypotheses for the formation of the two seamount clusters. Volcanism that produced these seamount clusters may have resulted from 1) off-axis upwelling of the Hawaiian mantle plume, 2) ancient arch volcanism (Bianco et al., 2005), 3) volcanism related to intra plate extension and deformation or 4) cretaceous hotspot volcanism.

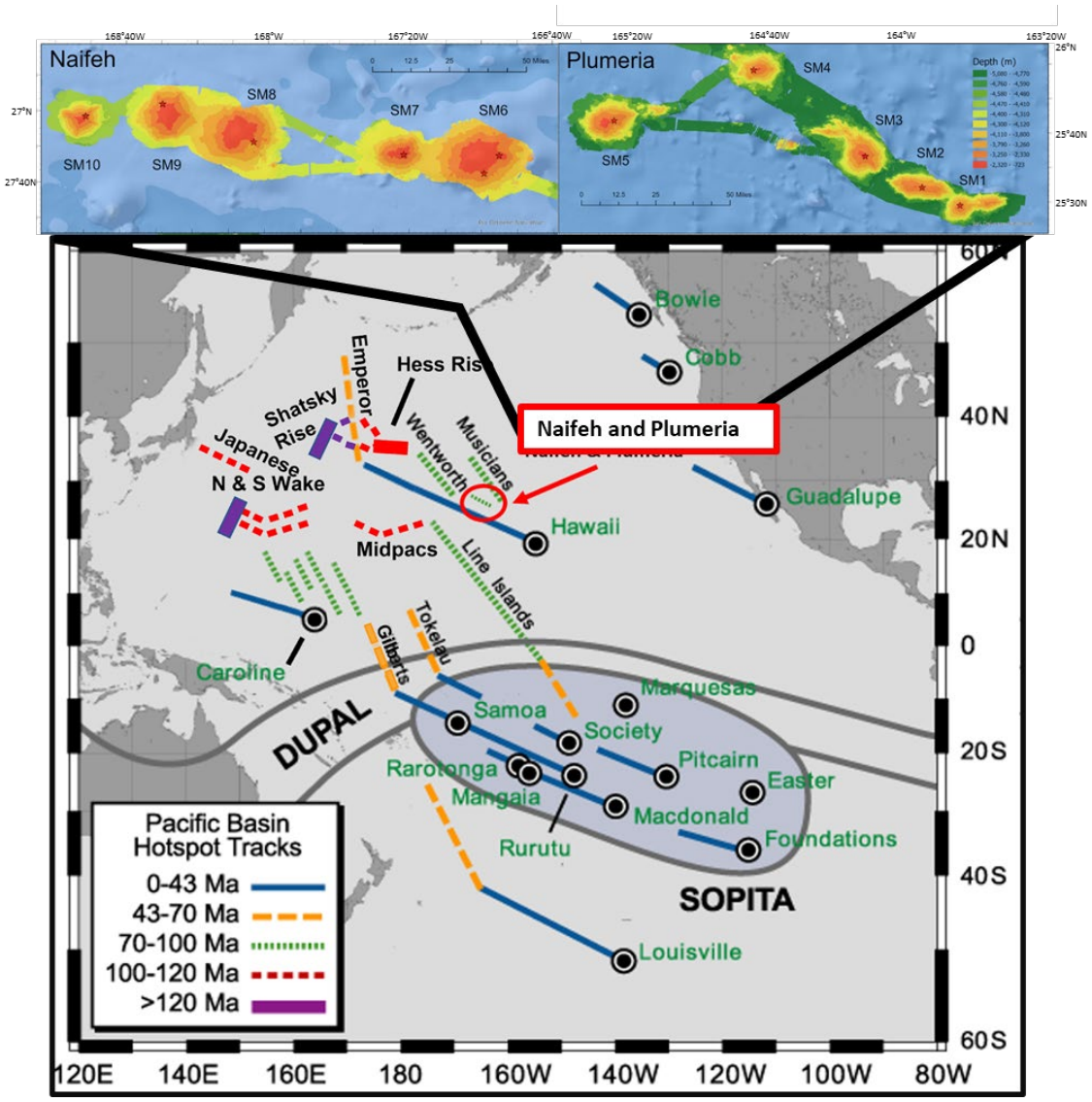

Figure 1. A map of seamount chains and their ages modified from Koppers et. al., 2012. Naifeh and Plumeria seamount chains circled in red.

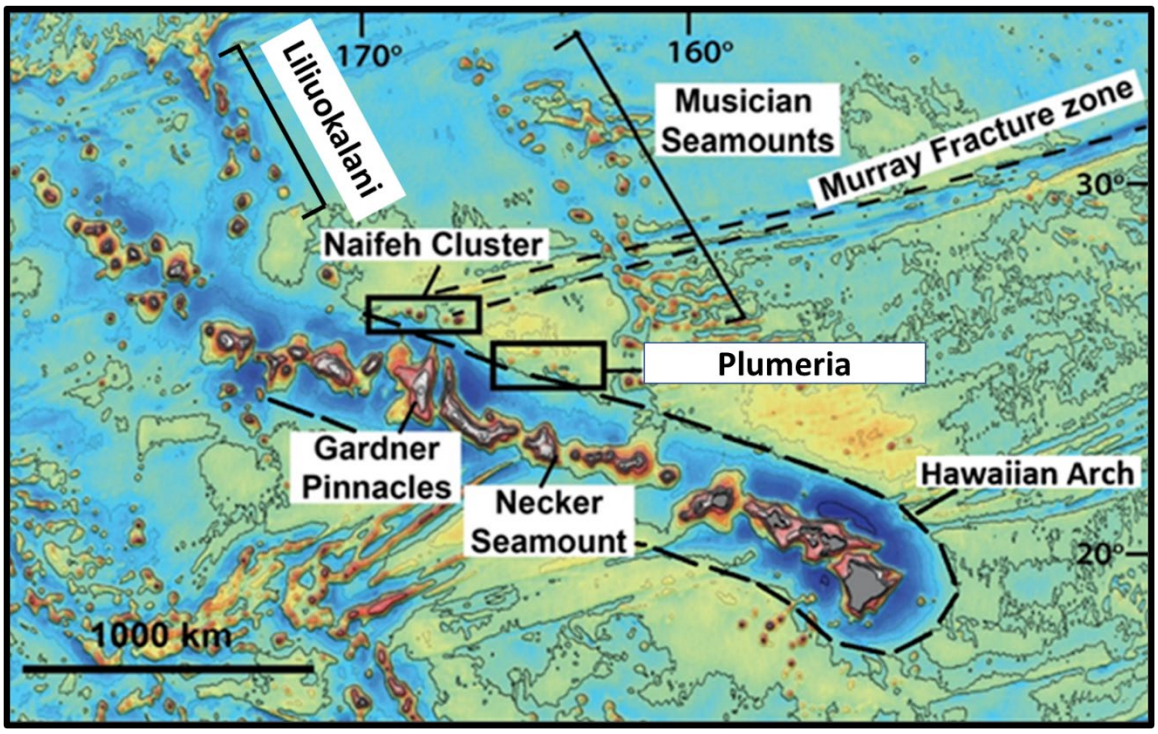

Figure 2. Marine gravity map of the region modified from Smith and Sandwell et al. (1997).

The Hawaiian-Emperor chain is the longest seamount chain in the Pacific basin at 5800 km in length. It is a classic example of primary hotspot volcanism commonly explained by upwelling and melting of a mantle plume (Wilson, 1963; Morgan, 1971). While the geochemistry of lavas from the main Hawaiian Islands has been intensely studied (Garcia et al., 2015, Sherrod et al., 2007; Garcia et al., 2010; Weis et al., 2011 and many more), the submarine portions of the chain are not as well characterized, especially lavas erupted off the main plume track. Lavas from the Naifeh and Plumeria chains could hold a wealth of information about the Hawaiian mantle plume or the upper mantle underlying the Pacific plate. However, the clusters are also positioned directly on the northern bulge of the Hawaiian arch (Figure 2). This suggests that the seamount clusters could be derived from Arch Volcanism, which forms through low degrees of melting from the flexing of the lithosphere caused by loading from the massive Hawaiian

volcanic structures (Bianco et al., 2005). If so, they would be the first studied examples of extinct arch volcanism (Frey et al.,2000; Lipman et al., 1989). A third hypothesis for the formation of the seamount clusters is that they form from intra-plate extension and deformation of the Pacific plate, similar to the nearby Musician seamounts (O'Connor et al., 2015). The Naifeh Cluster is situated at the end of the Murray Fracture Zone (Figure 2), suggesting that they could be related to extension and therefore, and have compositions similar to the nearby Musician Seamounts or depleted upper mantle. A fourth hypothesis is hotspot volcanism. The South Pacific Superswell has produced a large concentration of hotspots throughout the Pacific Ocean for the last 140ma, due to its relatively thin, hot lithosphere (Koppers et al., 2003, McNutt and Fischer, 1987; McNutt and Judge, 1990; Larson, 1991; Cazenave and Thoraval, 1994; McNutt et al., 1996, 1997; McNutt, 1998). These hotspots often produce thermally and isotopically anomalous lavas, giving it the name South Pacific Isotopic and Thermal Anomaly (SOPITA). Lavas originating from this superswell have high ratios of Pb isotopes that are attributed to subduction of crustal components into the mantle. (Koppers et al., 2003, Hofmann and White, 1982; White and Hofmann, 1982; Zindler and Hart, 1986; Staudigel et al., 1991). It is possible that Naifeh and Plumeria may have erupted from this region of the mantle depending on their age and composition.

Each of these mechanisms for formation may result in distinct geochemical signatures in the erupted lavas. This thesis aims to use major and trace element geochemistry to study the geochemical diversity of the Naifeh and Plumeria seamount chains and to interpret the tectonic and melting environments that produced these lavas. Previous studies from collaborators have indicated the lavas are 80-90ma using Ar/Ar

(Sotomayor et al., 2022), and have lead isotope data ranges $^{207}Pb/^{204}Pb$ 15.585-15.696, $^{206}Pb/^{204}Pb$ 19.369-20.065, and $^{208}Pb/^{204}Pb$ 39.251-39.779 (Cunningham et al., 2019). This thesis will address the following questions:

1. **Are these seamounts compositionally similar to the Hawaiian-Emperor chain, arch volcanism, or other local features such as the Musician seamounts? Are they similar to any other seamount chains in the South Pacific?**
2. **Are the Naifeh and Plumeria clusters chemically distinct from each other?**
3. **Are lavas from each individual seamount homogeneous, suggesting the seamounts are cogenetic? If not, what factors may contribute to chemical variability?**

METHODS

Sample Collection

Samples were collected from Naifeh and Plumeria by exploration vessel (E/V) Nautilus in September 2018 using the remotely operated vehicle (ROV) Hercules (Picture 1). The ROV made 11 dives to the seafloor with 1 dive per seamount apart from seamount 6, which was sampled at 2 locations (Figure 9). Each dive collected 4-8 rock samples. In total Hercules gathered 55 samples, of which 46 were suitable, or had enough fresh material for this study. Depths of sample locations range from 1258-2795m, with the surrounding seafloor at 4000-5000m depth. Bathymetric data was collected via a hull-mounted multibeam echosounder (Figure 1, 9).

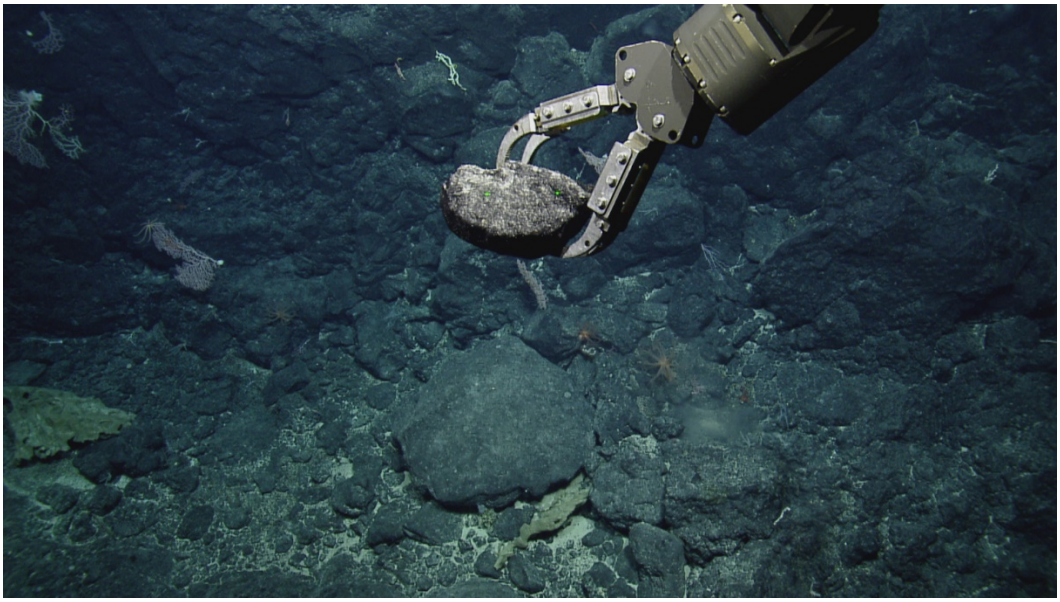

Picture 1. Digital still photo of ROV Hercules extracting a sample from the seafloor.

Major Element Analysis

Major element concentrations were measured for 27 whole-rock lava samples. Samples were cut with a rock saw to avoid altered material and manganese crusts. After cutting, the samples were sanded with a silicon carbide disk to remove any residue left from the saw blade. The samples were then crushed in plastic bags using a hammer and metal plate at Boise State University and then sieved to 1-2mm sized chips. Crushed rock chips were rinsed in an ultrasonic bath using a 1% hydrogen peroxide solution for 20 minutes to remove remaining fine particles, followed by repeated sonication in ultra-pure Milliq H_2O (18.2 MΩ) until water remained clear. Approximately 1–2 mm-sized cleaned chips were handpicked using a binocular microscope, avoiding phenocrysts and alteration. Samples were powdered using a ring mill with tungsten carbide surfaces. Major element contents were collected using a Rigaku Supermini Wavelength Dispersive X-ray Fluorescence (XRF) spectrometer at the University of Florida. Major element contents are presented in Table A1.

Trace Element Analysis

Method 1: Whole rock trace element contents were analyzed by solution ICP-MS at Boise State University following the procedures of Kelley et al. (2003) and Lytle et al. (2012). Approximately 50 mg of each sample from the clean chips prepared following the methods in the previous paragraph were digested in closed 23 mL Savillex Teflon beakers in 3 mL of 16M HNO_3 and 1 mL of 29M HF. Sealed capsules containing sample-acid solution were placed on a hot plate at ≤ 150 °C overnight (~ 12hr) until no trace of solids remained. Dissolved samples were then evaporated to dryness, uncapped on a hot plate, keeping surface temperature ≤ 100 °C until dry. Samples were redissolved and

dried 2x in 0.5ml 16M HNO_3. Finally, samples were re-dissolved in 3 mL of 16M HNO_3 and 3 mL of ultra-pure deionized H_2O in sealed capsules on a hot plate at ≤ 100 °C for ~ 12 h. The dissolved samples were transferred into 125 mL HDPE bottles for a 2500× ultra-pure milliq water (18.2 MΩ) dilution and sonicated for 30 min to ensure dissolution of all precipitates. Trace element concentrations were measured using a Thermo Scientific X-Series II Quadrupole Inductively Coupled Plasma Mass Spectrometer (ICP-MS) coupled with an ESI SC-FAST autosampler. Samples were corrected using an internal standard solution containing 5ppb In, blank corrected using a procedural blank, drift corrected using periodic measurements of Geological Survey of Japan (GSJ) standard JB-3, dilution weight corrected, calibrated using US Geological Survey (USGS) standards, GSJ standards, and internal laboratory standards: BHVO-2, BIR-1, DNC-1, W-2 (USGS), JB-3 (GSJ), and 2392-9 (University of Florida in-house standard; Goss et al., 2010). 35 lavas were analyzed for trace element contents using method one. Trace element contents from method 1 are presented in Table A2.

Method 2: Whole rock trace element contents were analyzed by solution ICP-MS at Boise State University following the procedures of Kelley et al. (2003) and Lytle et al. (2012) at 1/10th scale. This procedure was run for samples without sufficient quantities of fresh, unaltered material. Approximately 5 mg of each sample were digested in closed 23 mL Savillex Teflon beakers. The procedure is the same as method one, except the dissolution was run at 1/10th of the quantity of HNO_3, HF, and MilliQ H_2O. Trace element concentrations were measured using a Thermo Electron X-Series II Quadrupole Inductively Coupled Plasma Mass Spectrometer (ICP-MS) coupled with an ESI SC-FAST autosampler. Samples were corrected using an internal standard solution

containing In, blank corrected using a procedural blank, drift corrected using Geological Survey of Japan (GSJ) standard JB-3, dilution weight corrected, calibrated using US Geological Survey (USGS) standards, GSJ standards, and internal laboratory standards: BHVO-2, BIR-1, DNC-1, W-2 (USGS), JB-3 (GSJ), and 2392-9 (University of Florida in-house standard; Goss et al., 2010). 15 lavas were analyzed for trace element contents using method two, with 5 samples run as duplicates from method one as a quality check for this procedure. Trace element contents from method 2 are presented in Table A3.

RESULTS

Major and Trace Element Geochemistry

To measure the heterogeneity of the Naifeh and Plumeria seamount chains, major and trace elements contents were analyzed for one to ten lavas from each of the 10 seamounts. Samples are classified according to their igneous rock types using the total alkali (K2O + Na2O) vs silica (TAS) diagram from Le Maitre et al. 1989 (Figure 3). The TAS diagram is divided into tholeiitic and alkaline compositions by the MacDonald and Katsura line from MacDonald and Katsura (1964). The lavas from the Naifeh and Plumeria seamounts have SiO_2 ranging from 48.4-55.01 wt % and total alkalis 5.19-8.74 wt%, thus they are all alkalic and range from Trachybasalt to Trachyandesite (Table A1). Loss on ignition (LOI) values range from 1.24% to 4.19% with an average of 2.70%.

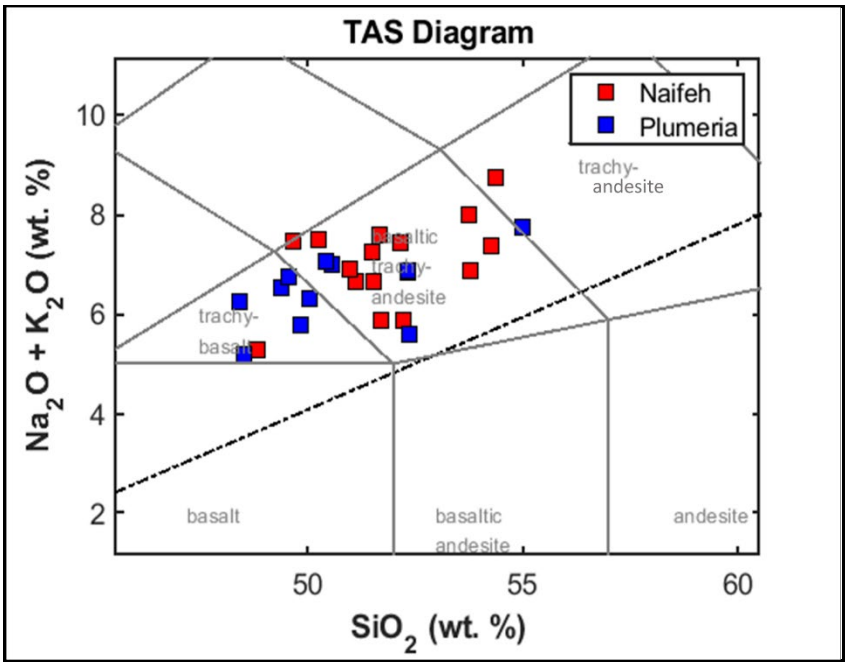

Figure 3. Total Alkalis versus Silica diagram for the Naifeh and Plumeria seamounts.

Figure 4 shows the major element data from the Naifeh and Plumeria lavas vs MgO. There is a slightly positive correlation between CaO (4.66-10.58 wt%), and MgO (0.73-2.82 wt%), and negative correlations between MgO and Na_2O (2.0-5.17 wt%); K_2O (1.63-4.26 wt%) and Al_2O_3 (17.6-23.88 wt%). There are no trends with MgO and SiO_2, FeOT (3.04-13.58 wt%, MnO (0.018-0.151 wt%) or P_2O_5 (0.52-4.61%).

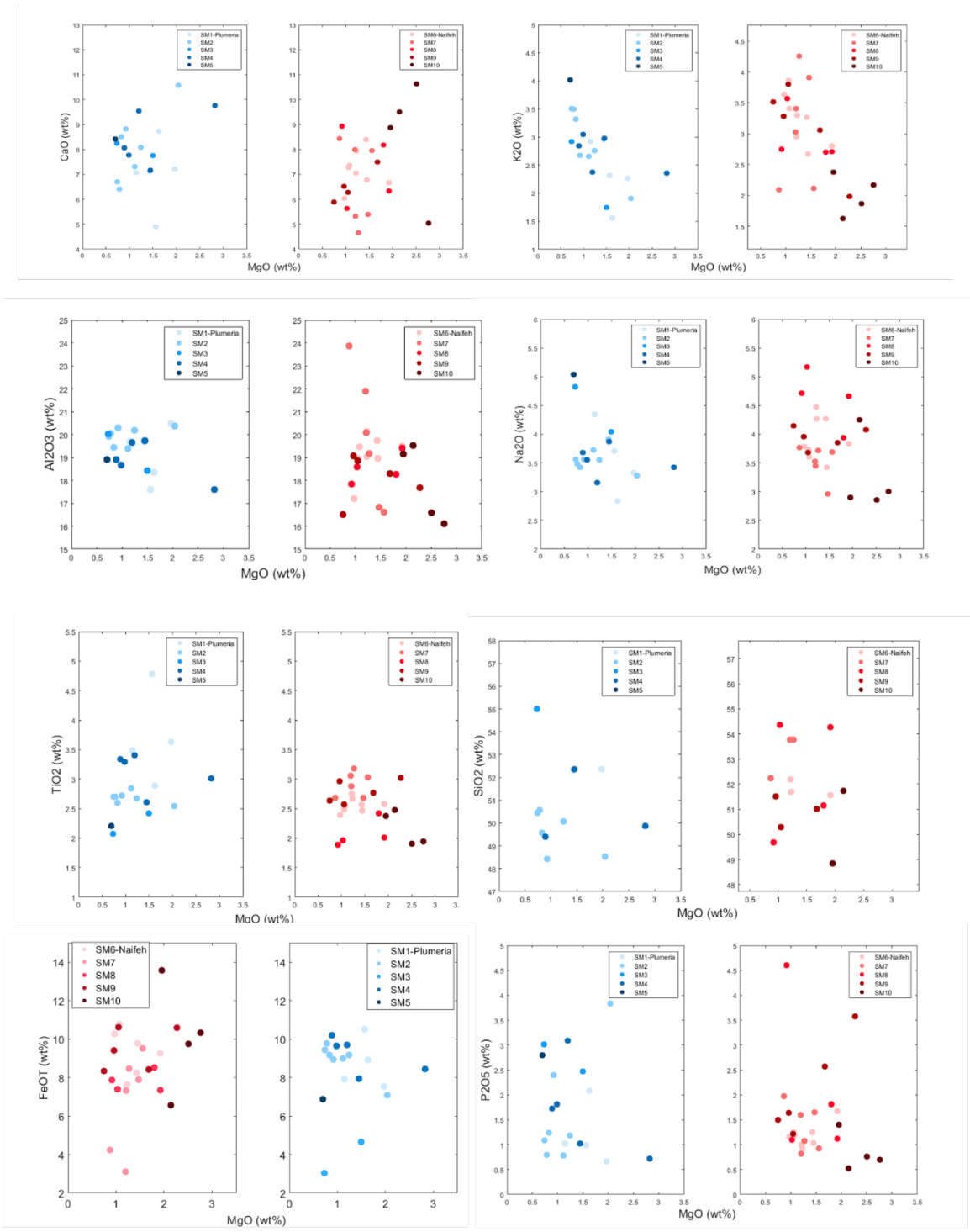

Figure 4. Harker Diagrams of Major Element vs MgO (wt%). Lavas from plumeria are plotted with blue markers, Naifeh lavas plotted with red markers. Different shades of red and blue markers indicate different seamounts.

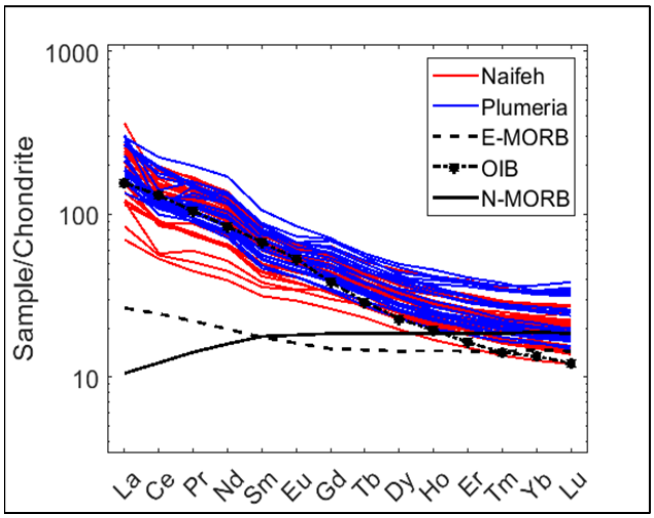

Figure 5. REE diagram of Naifeh and Plumeria seamounts with average OIB, N-MORB, and E-MORB from Mcdonough & Sun 1995. Whole rock ICP-MS data normalized to chondrite (McDonough et al., 1992).

The Naifeh and Plumeria seamount lavas are generally enriched in their light rare earth element (LREE) concentrations similar to average ocean island basalt (OIB) composition from Mcdonough and Sun (1995) but break the pattern with more enriched heavy rare earth elements (HREEs) than OIB. The seamounts are inconsistent with average normal mid-ocean ridge basalt (N-MORB) or enriched mid ocean ridge basalt (E-MORB) rare earth element (REE) compositions (Figure 5). Most of the lavas have relatively smooth patterns in REE; however, several have a steep drop in cerium concentrations known as a negative cerium anomaly (Figure 5 & 6). While the overall patterns are similar for many of the seamount lavas, the total concentrations of the REE are variable.

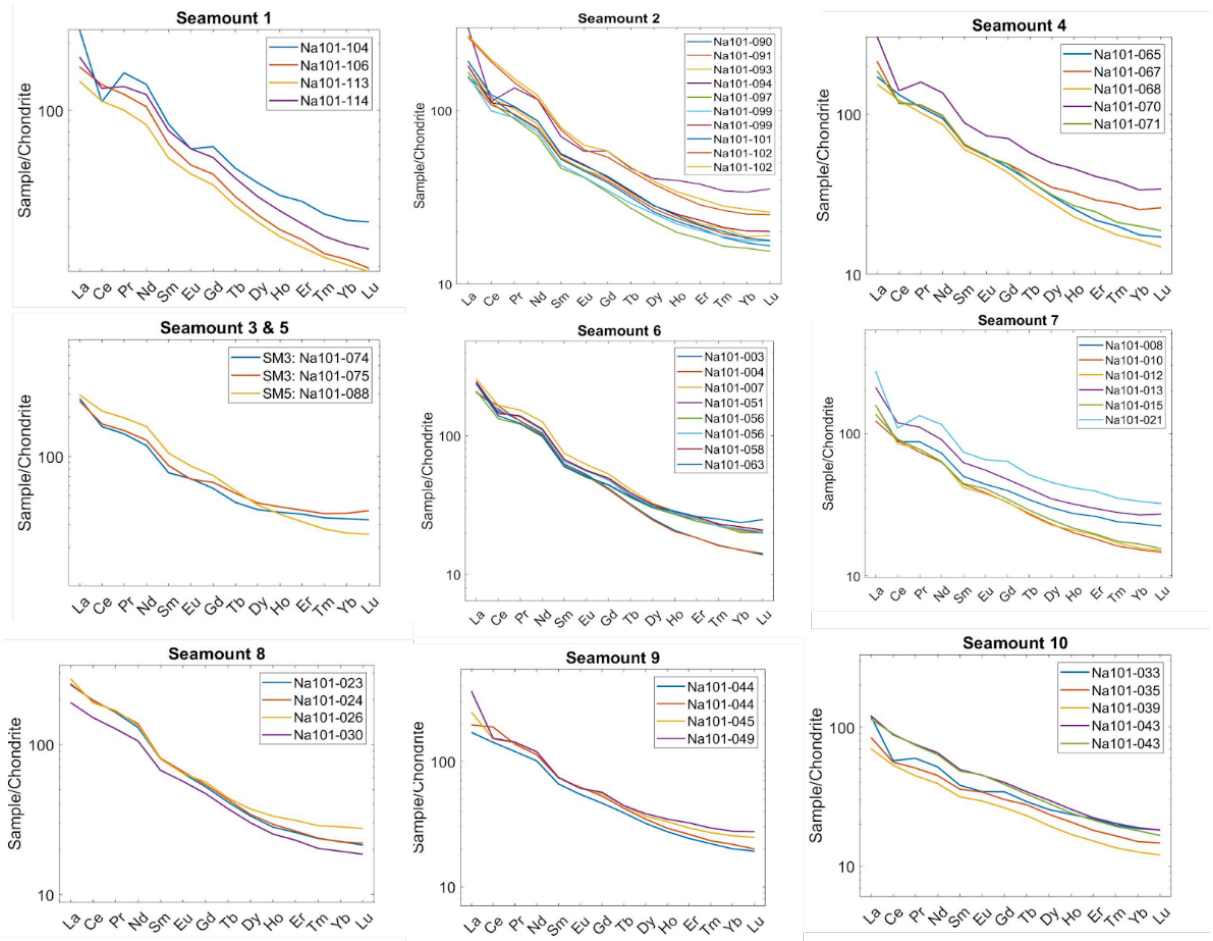

Figure 6. REE patterns by seamount. Data normalized to chondrite (Mcdonough et al., 1992). Seamount 3 (N101-074 & 075) and 5 (Na101-088) plotted together due to the low number of samples for each.

DISCUSSION

The Effects of Alteration on Major and Trace Elements

Submarine volcanic rocks exposed to seawater for tens of millions of years will have some level of alteration affecting their bulk chemical composition (Staudigel et al., 1996). The seamount samples have variable alteration due to the growth of ferromanganese crust, filling of vesicles by secondary minerals, and the transformation of olivine to iddingsite. Furthermore, no volcanic glass was observed on any of the samples. The addition of clay and zeolite minerals can increase the alkali content of tholeiitic lavas (Hart and Staudigel, 1982), making them appear alkalic, but because all samples are alkalic and are defined by a narrow range of compositions, it is not likely major element compositions were affected by alteration aside from FeOT, P_2O_5, and MnO wt% due to the presence of ferromanganese crusts.

Fluid mobile trace elements Cs, Rb, and U are sensitive to seawater alteration, while high field strength elements (HFSEs) Nb, Ta, Hf, Zr, Y, Ti, and Th and REEs La through Lu are relatively immobile and less sensitive to alteration. A negative Ce anomaly is a known characteristic of (oxidized) seawater altered basalts (Dürkefälden et al., 2021; Bellot et al., 2018). Thus, negative Ce anomalies and in particular La/Ce ratios can be used to identify samples that have been altered. Samples 033, 049, 104, 094, 067, 070, 021, 012, and 008 display such anomalies, with a La_n/Ce_n value above 1.8 (Figure 7), which has been used as a cut-off for significant alteration. Based on this, these samples have been filtered out of the dataset due to alteration and are not included in any

statistical analyses. These samples are shown in figure 6 and 7 to highlight the variation in REE patterns but are not shown in any of the other geochemical plots. Sample Na101-002 was also filtered out due to Ce anomaly, and values for REE were 10X above the rest of the data. Lavas Ce anomalies can be seen in figure 6, REE patterns without Ce anomalies presented in Figure 8.

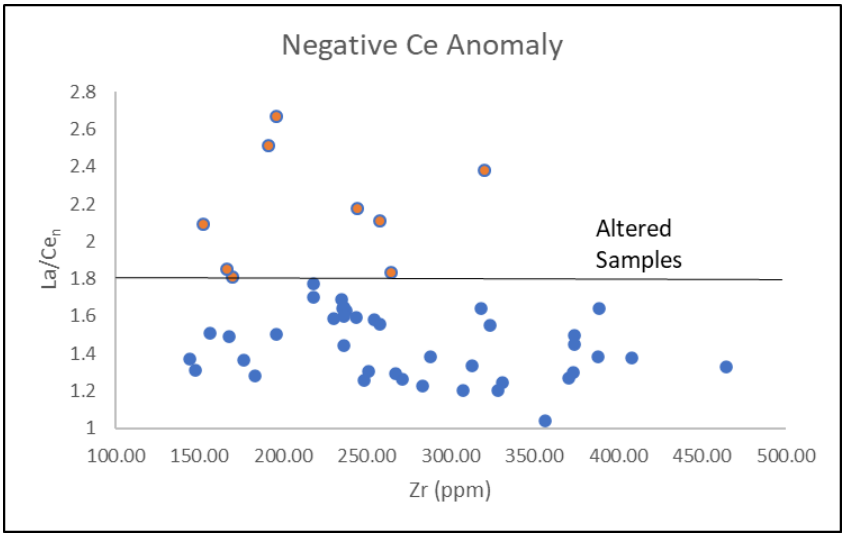

Figure 7. La/Ce normalized to chondrite (Mcdonough et al., 1992) vs Zr. Negative cerium anomaly is most easily observed in samples above 1.8 La/Ce(n).

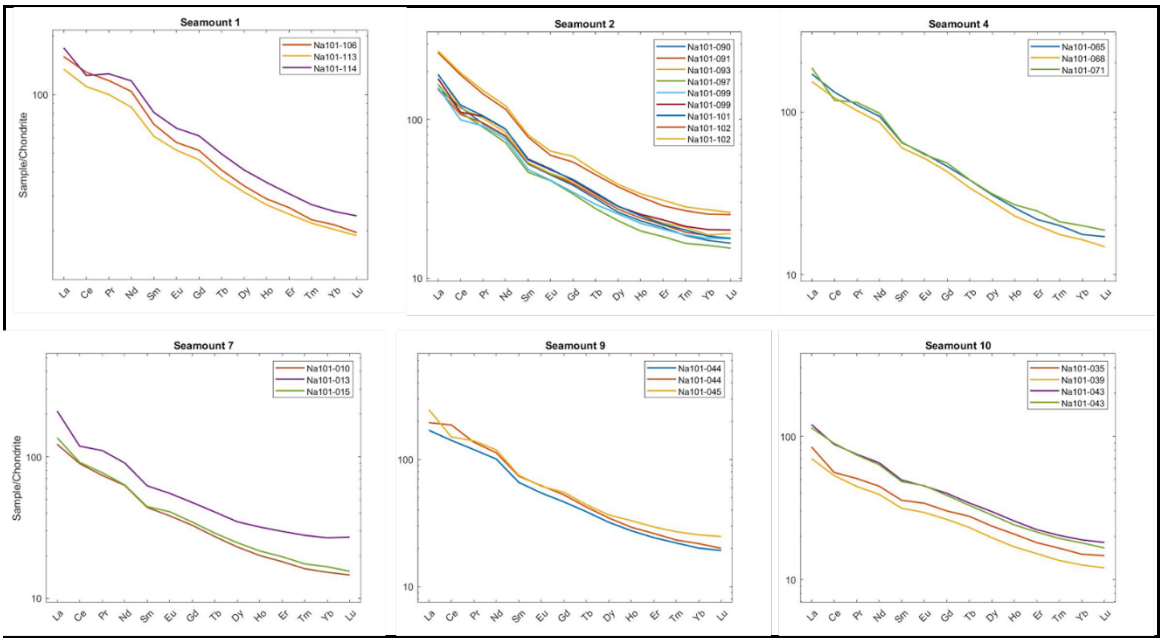

Figure 8. REE patterns by seamount after removing samples with Ce anomaly. Data normalized to chondrite (Mcdonough et al., 1992). Seamounts 3, 5 and 6 had no Ce anomalies, and are presented in Figure 6.

Bathymetric Mapping and Volcanic Morphologies

Both the Naifeh and Plumeria chains consist of five individual seamounts (Figure 9). The Naifeh chain trends from East to West, while the Plumeria chain trends slightly more NW to SE except for seamount five which is off-set further west than the rest of the volcanoes in Plumeria (Figure 9). The seamounts rise 2-4 kilometers above the surrounding seafloor, suggesting considerable erupted volumes.

Bathymetric mapping of the two seamount chains shows heterogeneous morphologies of the individual seamounts within the Naifeh and Plumeria chains (Figure 9). The morphology of seamounts is affected by the size, geometry, and migration of their magma conduits, eruption rates and viscosity of magmas, crater or caldera development, basement topography, regional gravitational stress, and erosion (Schmidt and Schmincke, 2000; Hunt and Jarvis, 2020). Mapping conducted in 2018 by the

exploration vessel Nautilus revealed that SM6, SM8 and SM9 (Figure 9) are guyots. The flat-topped nature of these two seamounts indicates that they breached the sea surface and erupted large volumes of lava. Seamounts from the Naifeh cluster consist of sub-circular (seamount 6, 7, 8 and 9) to star-shaped (seamount 10) volcanoes. Stellate morphologies preserve radial dyke intrusions despite considerable gravitational slope failure (Bulmer & Wilson, 1999). The Plumeria cluster has more elongated volcanic structures (seamounts 1 and 2) that stretch in the NW-SE direction. Elongation could be due to eruption along a zone of weakness in the crust such as a fracture zone (Richards et al., 2018).

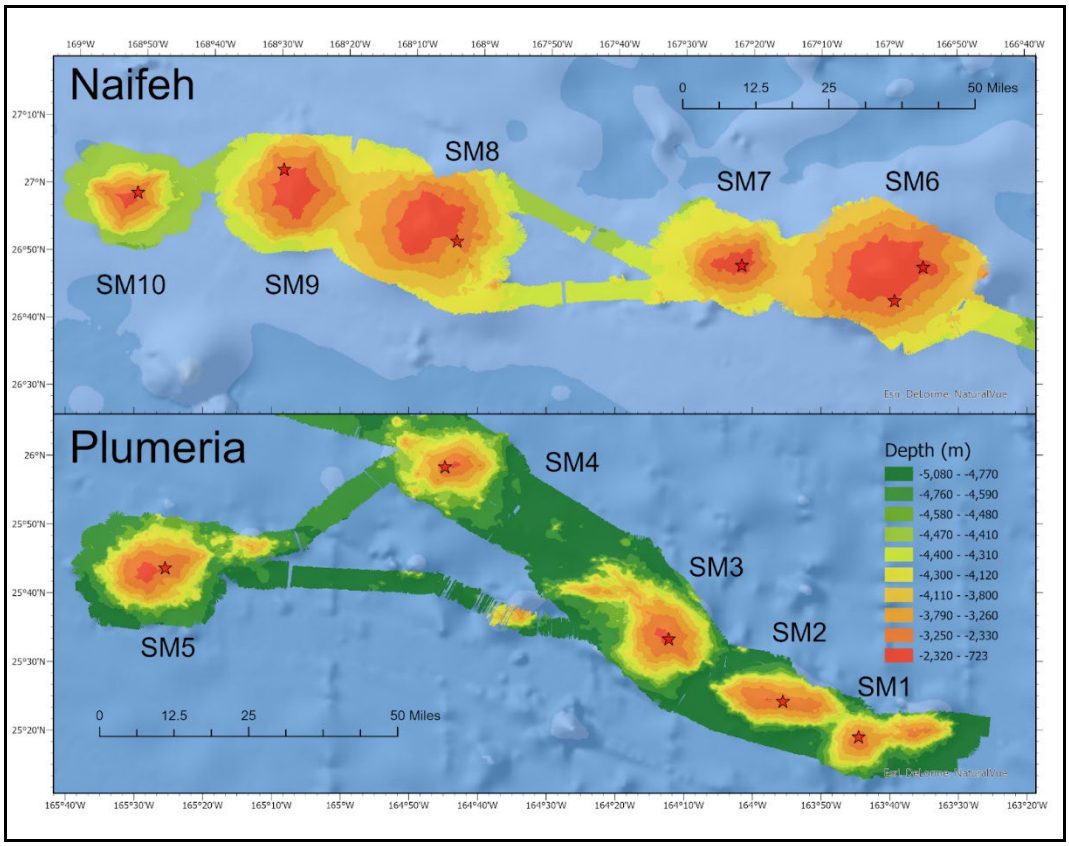

Figure 9. Bathymetric maps of Naifeh and Plumeria seamount chains. Data collected using a hull mounted multibeam system on the EV Nautilus.

Chemical Variation between Naifeh and Plumeria Clusters

The Pacific plate contains many individual seamounts and short seamount chains, in addition to the larger, longer lived Hawaiian style chains (Koppers et al., 2003). The location and orientation of Naifeh and Plumeria may suggest that they may be part of a single seamount chain with one distinct origin, or that they are each distinct chains with different origins. Below I use rare earth elements to first evaluate if the two clusters of seamounts are similar in composition, to second determine if there is any systematic variability with geographic location along the chains, and finally, I evaluate if there are any distinct chemical compositions within an individual seamount.

When comparing the compositions from the two clusters, a slightly higher enrichment in the median values of REEs in lavas from the Naifeh cluster compared to Plumeria is observed (Figure 10). This is true for all elements except Tb and Dy, which are nearly identical in median value. Despite the overall enrichment of the Naifeh chain relative to Plumeria, the ratios of LREEs vs HREEs for each cluster (Figure 11) are indistinguishable.

To further quantify this variability, a Kolmogorov–Smirnov (KS) test was performed with the KStest2 function in MATLAB. Using LREE ratios of Naifeh vs Plumeria, the null hypothesis that the two datasets were from the same distribution was not rejected at a 5% significance level, with a P value of 0.9735. The same test was performed on the heavy rare earth element ratios and the result was the same with a P value of 0.7383. These results suggest that two datasets occupy the same distribution (Figure 12) and therefore we conclude the Naifeh and Plumeria seamount chains are statistically similar in REE ratios, but have slightly different REE compositions, with the Naifeh compositions having higher concentrations. This likely suggests that the two chains are from the same mantle source but have undergone various extents of crystallization or extents of melting. This is discussed further later in the discussion section.

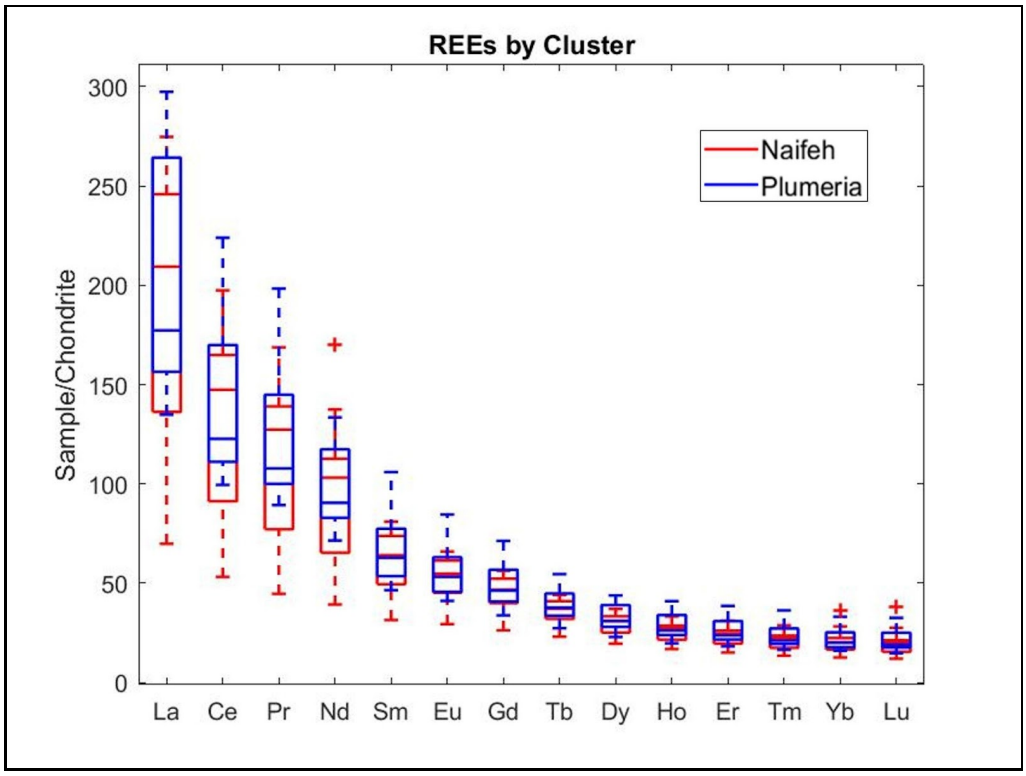

Figure 10. Boxplots for rare earth elements normalized by chondrite (Mcdonough et al., 1992) for all samples within the Naifeh cluster vs all samples from the Plumeria cluster. The Naifeh cluster is indicated by the red boxplots, and Plumeria is indicated by the blue boxplots. REEs normalized by Chondrite (Mcdonough et al., 1992).

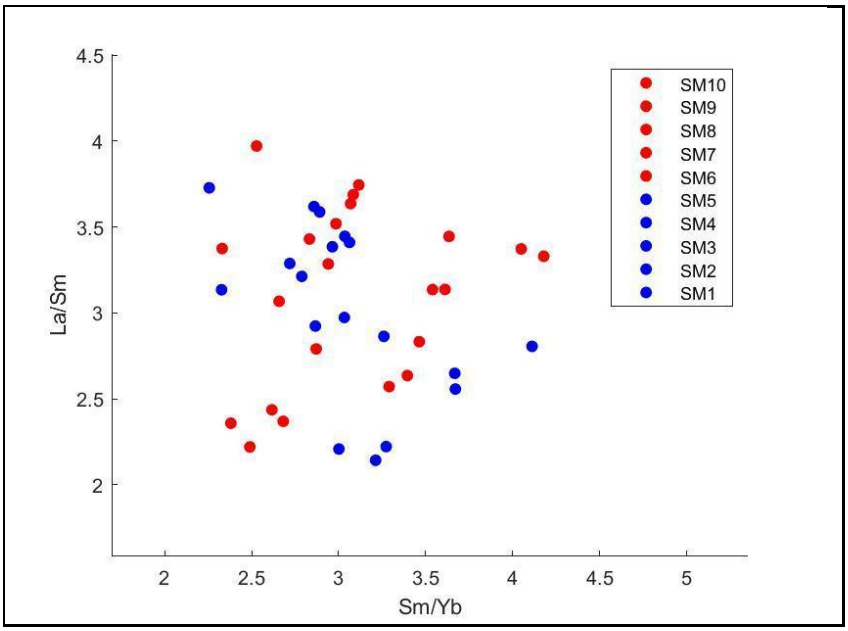

Figure 11. Naifeh (SM10-6) and Plumeria (SM5-1) seamount chains LREEs vs HREEs normalized to Chondrite (Mcdonough et al., 1992).

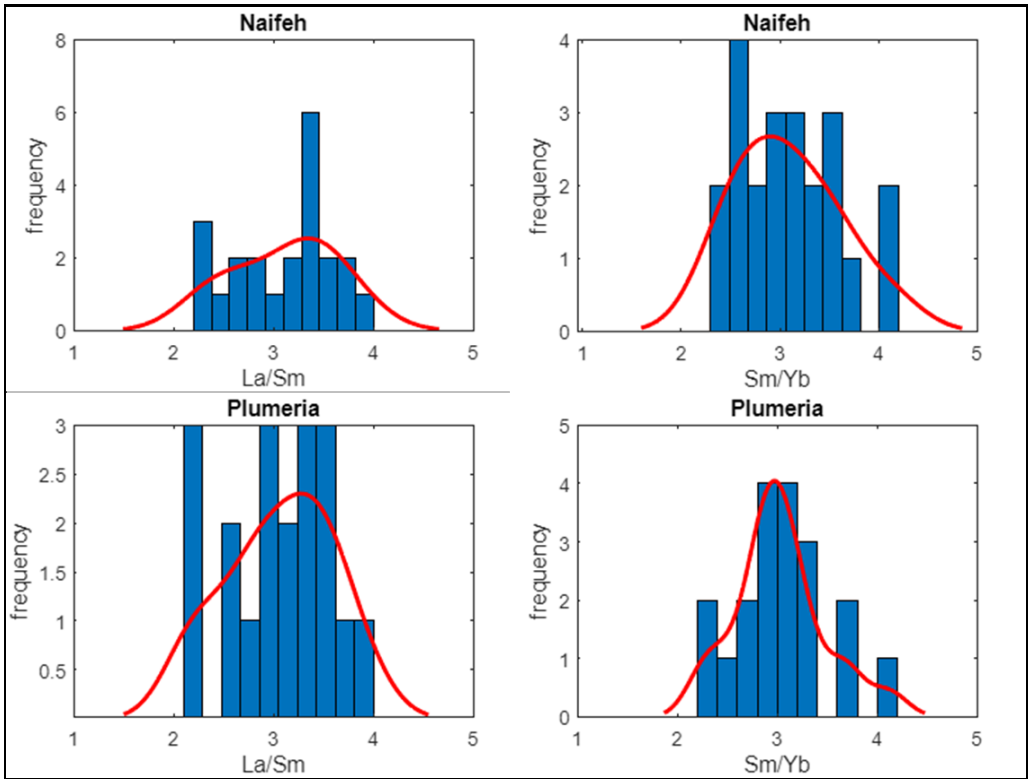

Figure 12. Histograms showing the frequency of Light rare earth element ratios for each cluster on the left and heavy rare earth elements for each cluster on the right. A bisquared kernel weighted function was applied to the data and plotted as a red line. Samples are normalized to chondrite (Mcdonough et al., 1992).

We next investigate if there is any systematic variability in composition along the two seamount chains geographically. The Naifeh cluster shows a systematic increase in median LREE ratios from west to east (Figure 13 & 14). There is also a systematic increase in median values in HREEs, with the exception of Seamount 7, which has lower median values. There is no systematic variation in LREE and HREE ratios from the Plumeria cluster (Figure 13 & 14) from east to west. This suggests that there may be a slight change in the mantle source or extent of melting with distance along the Naifeh chain, but similar variability is not observed within the Plumeria seamounts.

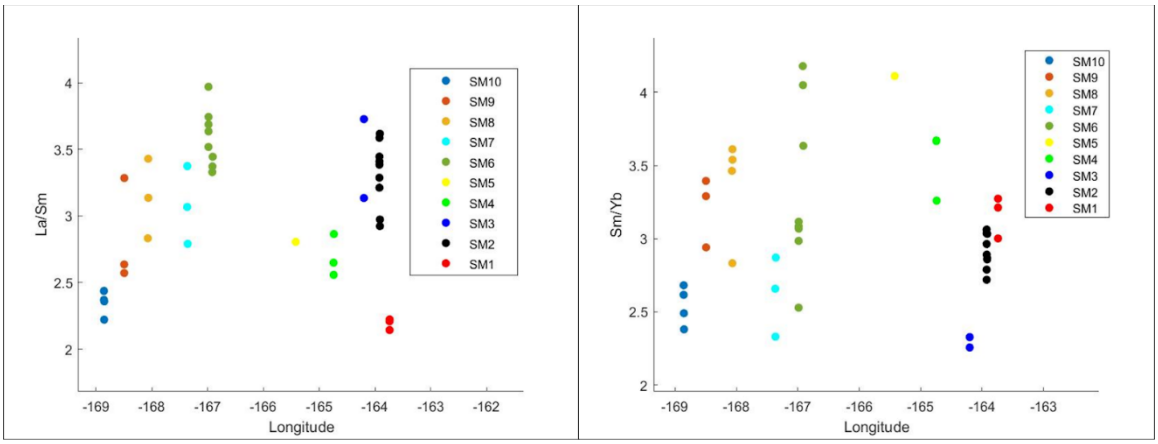

Figure 13. Variation in LREE (A) and HREE (B) ratios by Latitude along the Naifeh and Plumeria chains. SM10-SM6 are from the Naifeh chain, SM5-SM1 are from the Plumeria chain. Data is normalized to chondrite (Mcdonough et al., 1992).

Finally, I investigate the chemical variability between individual seamounts. There is some chemical variability within each seamount in LREE and HREE ratios, which is evident in the trace element ratios and the boxplots of each seamount (Figure 14). Furthermore, boxplots for each seamount show that lavas from seamounts 1 and 10 have lower median LREE ratios than the rest of the seamounts (Figure 14). Median HREE ratios for seamounts 10, 7, and 3 are lower than the rest of the seamounts (Figure 14).

Combined these results suggest that each seamount has its own magmatic history. The variation in rare earth element contents may be due to fractional crystallization, heterogeneous mantle source compositions, and/or changes in the degree of partial melting. The role of fractional crystallization and partial melting will be investigated respectively in the following sections.

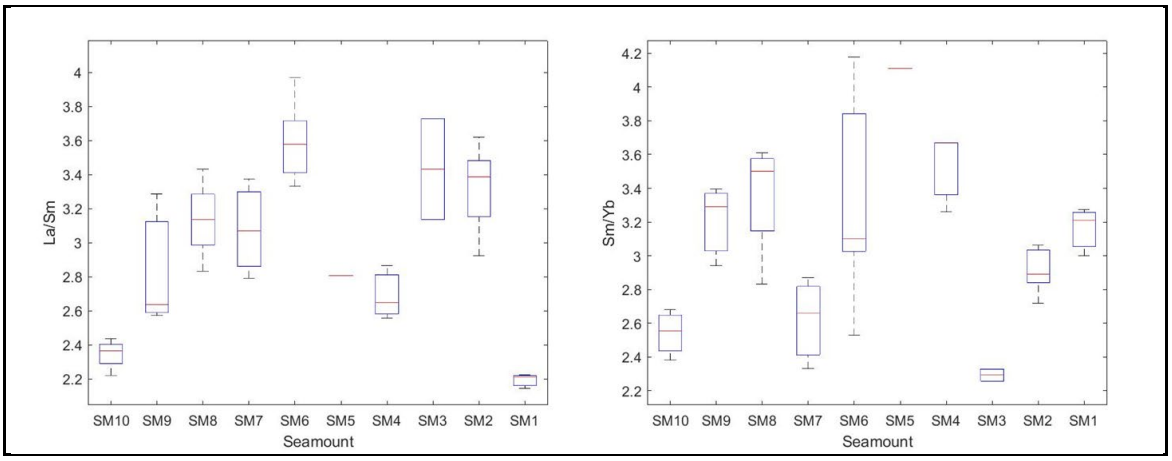

Figure 14. Box plots of LREE (Left) and HREE (Right) for each seamount. Samples are normalized to chondrite (Mcdonough et al., 1992).

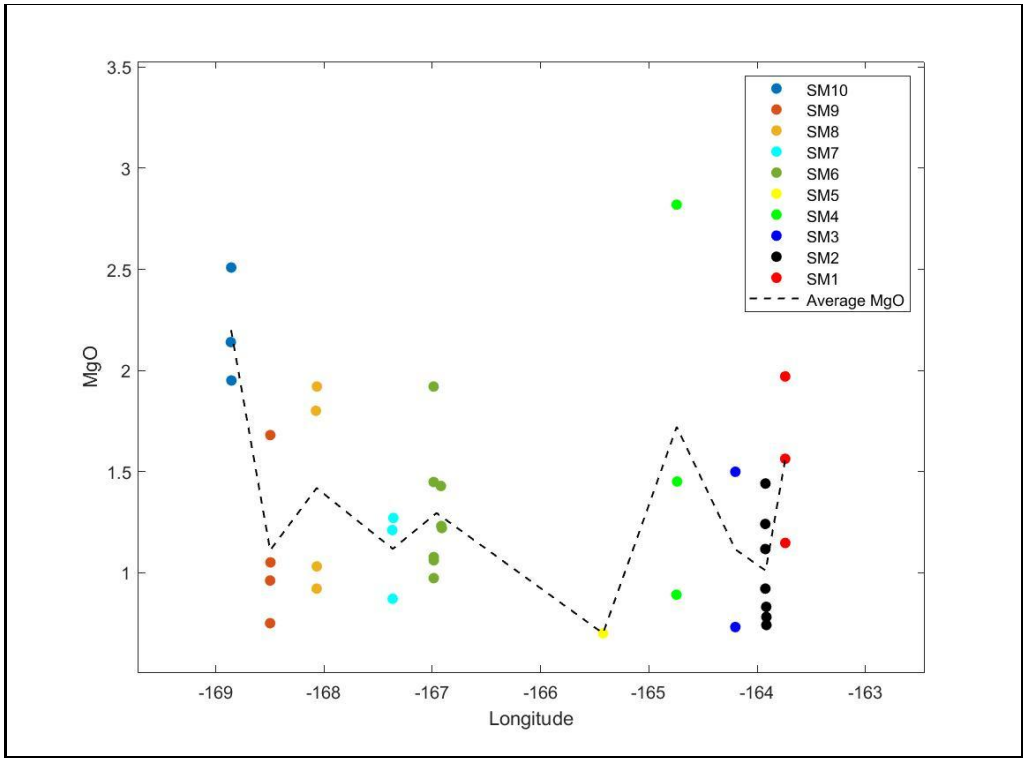

Figure 15. MgO (wt%) contents by longitude, black dashed line representing the average values from east to west.

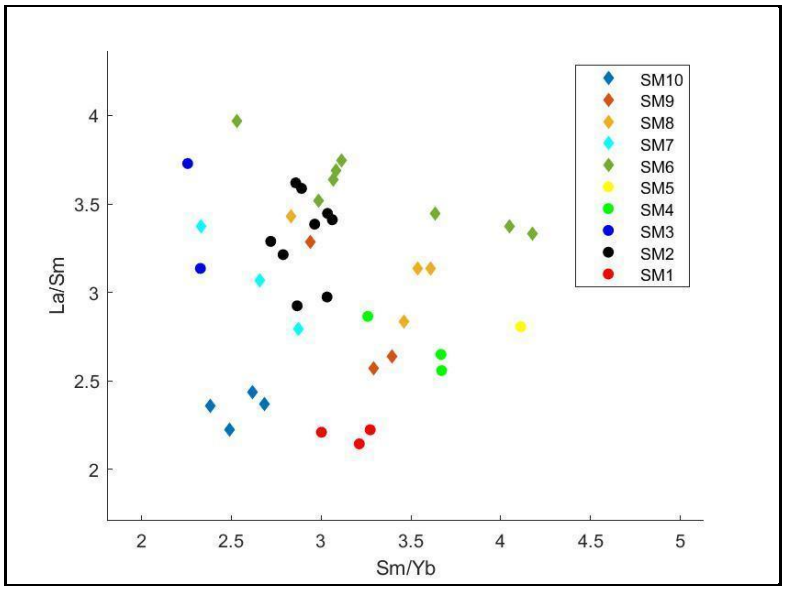

Figure 16. LREE vs HREE ratios for each seamount normalized to chondrite (Mcdonough et al., 1992).

Fractional Crystallization

Major element compositions in basaltic melts can be highly influenced by fractional crystallization of mineral phases such as olivine, CPX and plagioclase (Winter, 2010). In general, fractional crystallization of Olivine will cause a decrease in MgO and FeO contents, plagioclase crystallization will lower Al_2O_3 and CaO, and CPX crystallization will decrease CaO, CaO/Al_2O_3, and MgO. However, pressures of crystallization and water content can also influence crystallizing phases and when crystallization begins. Here we investigate the extents and depths of crystallization of lavas from each of the seamounts using petrologic modeling.

To quantify the extents and depths of crystallization, liquid lines of descent were calculated using the petrologic modeling software Petrolog3 (Danyushevsky & Plechov, 2011). A series of petrologic models were run for each of the seamounts. While it is not likely that the lavas from different seamounts crystallized from a single parental magma, the limited range of MgO contents made modeling challenging. Thus, the most primitive

lava in the dataset (MgO wt% content of 2.82 wt%; sample NA101-68) was used as the parent magma (Figure 15). The oxygen fugacity was set at QFM, the starting water content was varied from 0 to 3 wt%, and the pressures of crystallization were varied from 3-10 kbar.

Major element contents are best reproduced by fractional crystallization from 3-10kbar (Figure 17), but due to the low MgO contents, varying the pressure did not change the liquid lines of descent noticeably. However, varying H_2O content produced the biggest change in liquid lines of descent. Using a water content of 0.5% H_2O provided the best fit to the data. These models suggest ~25% crystallization of clinopyroxene alone can account for some of the compositional variability. Interestingly, the starting MgO wt% is too low to crystallize olivine. An increase in Al_2O_3 with decreasing MgO (in both the whole rock data and the petrologic models) is consistent with a lack of fractional crystallization of plagioclase, as well as a lack of Europium anomaly in REE diagrams (Figure 6).

While the model presented is the "best fit" to explain the major elements, it does not explain the range of compositions observed. Thus, multiple parent magmas are required to produce the variation in data. This is not unexpected, as these lavas erupted at numerous seamounts 100s of kms apart with up to 4km in relief. To determine if the major element contents of lavas erupted at a single seamount can be explained by fractional, I use Seamount 4 as a case study. While it would be better to model all seamounts individually, our limited dataset and the range of MgO contents made modeling fractional crystallization at all seamounts difficult.

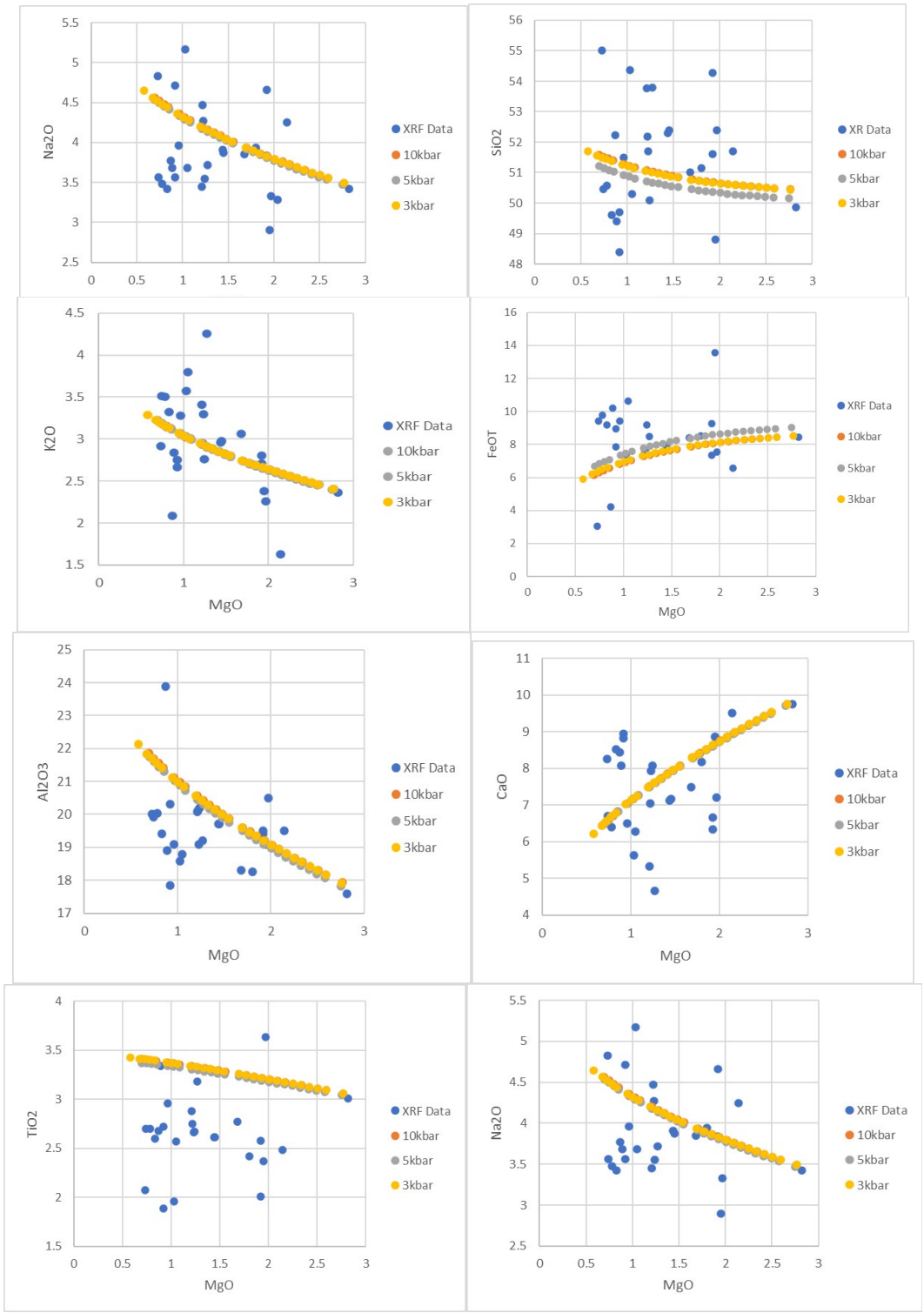

Figure 17. Fractional crystallization models made using Petrolog 3. XRF data for all seamounts from Naifeh and Plumeria are plotted with the most primitive sample used as the starting composition for fractional crystallization. Crystallization of CPX was modeled for 3, 5, and 10 kbar pressure at 0.5% H2O.

Seamount 4 was used to investigate the role of crystallization in producing the range of major element composition because it has the largest variation in MgO content (0.89-2.82 wt%). Major element data from XRF and ICP-MS are plotted in Figure 18. Fractional crystallization was again modeled with Petrolog3 (Danyushevsky & Plechov, 2011), using QFM as a buffer. Pressures were varied from 1-5kbar, but again had little effect on the model results. H_2O contents were varied from 1-3%. Changing the water content resulted in liquid lines of descent with lower major element concentrations vs MgO as starting H_2O percent was increased. However, variations in water content alone cannot account for all of the variability in the data, suggesting that multiple parent magmas are required to explain the range of compositions. Seamount 4 is ~3000m tall and ~40km wide; thus, it is not surprising that it consists of multiple lava flows with multiple parent magmas.

The petrologic modeling of fractional crystallization from all the seamounts and the case study of Seamount 4 suggests that fractional crystallization can account for some of the variation in major element compositions. Fractional crystallization will also increase the overall concentration of REEs in a magma, as REEs are incompatible in many of the crystallizing phases, except for Eu in Plagioclase. REE patterns in the seamount lavas are relatively similar (Figure 5), suggesting that the variations in concentration may result from fractional crystallization. This process may also account for the higher median concentrations of REEs in the Naifeh seamounts compared to Plumeria, with Naifeh experiencing slightly greater extents of crystallization.

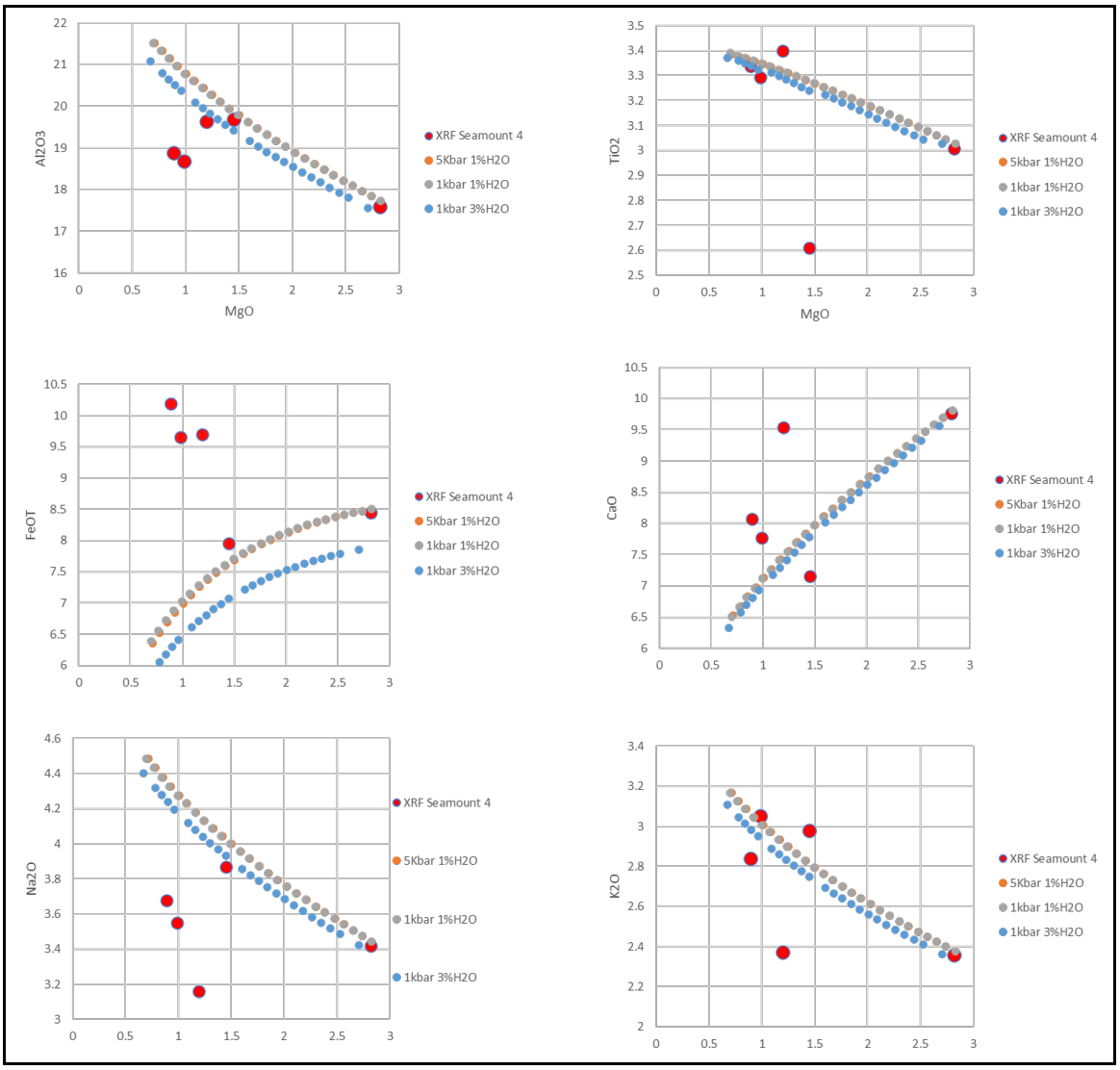

Figure 18. Petrolog 3 Fractional crystallization models for seamount 4. Orange, gray, and blue lines represent fractional crystallization of CPX with varying H2O and pressure. Yellow lines represent fractional crystallization of CPX and Pigeonite.

Fractional crystallization can increase the overall concentrations of REEs in a melt (Winter, 2010). To investigate if REEs are being concentrated by this mechanism, I modeled fractional crystallization to determine if this process can account for the range of concentrations in all of the seamounts (Figure 19). Using the formula $C_l = C_o * F \text{ ^}(D-1)$, and the initial concentration of trace elements in the source (C_o) and caluclated the

concentration of the trace elements in the melt (C_l) after a fraction (F) of the melt has crystallized using the element's partition coefficient (D). The sample with the least concentrated REE's (NA101-039) was used as the primary melt, and crystallized from 20-80%. The model (Figure 19) demonstrates that 20-80% fractional crystallization of 20% plagioclase, 60% CPX, and 20% Olivine produces melts that have parallel trends and span the range of REEs of the Naifeh and Plumeria lavas suggesting that fractional crystallizaiton may be responsible for the range of concentrations observed. However, 80% fractional crystalliztion of a melt is difficult, so it is still likely that multiple parent magmas are needed to explain the Naifeh and Plumeria REE compositions.

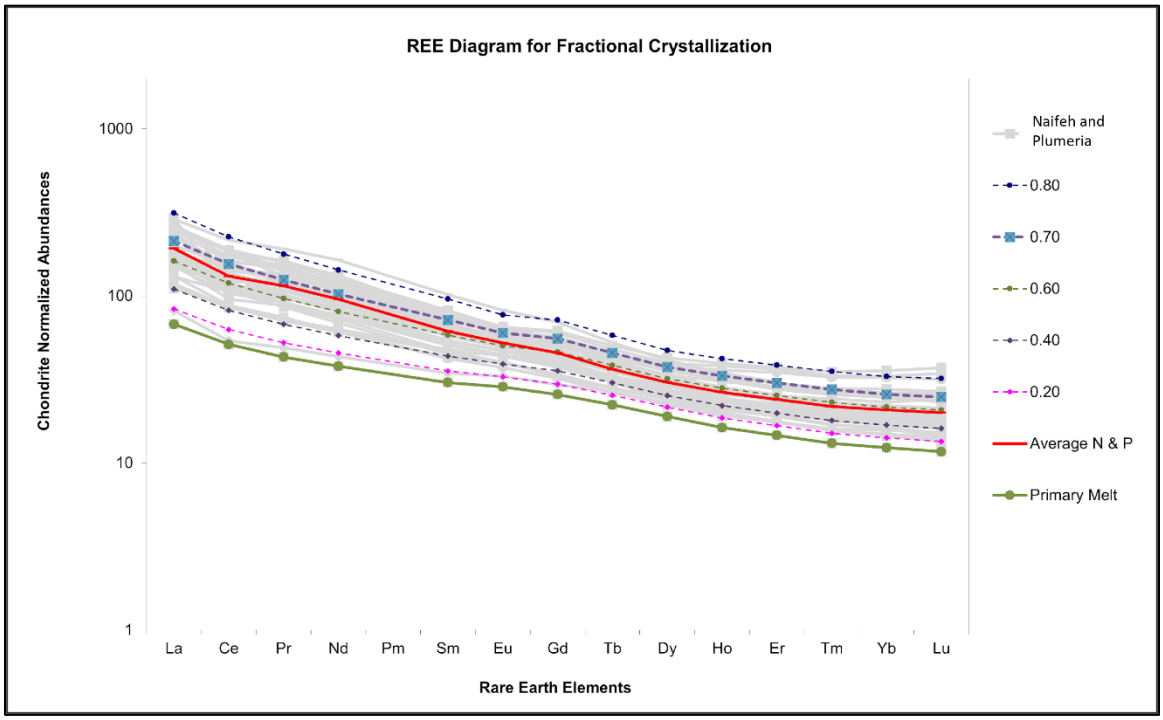

Figure 19. REE fractional crystallization model using sample NA101-039 as the primary melt. Fractional melts from 20-80% crystallization are shown by colored lines, Naifeh and Plumeria data represented by gray lines with the average REE concentration shown by the red line.

An alternative way to investigate role of fractional crystallization is to determine if a single parent magma can explain the range of concentrations at a single seamount. To

study the extent of fractional crystallization of one parent magma I ran the same model and compared it to lavas erupted at only one seamount (Figure 20). Seamount 2 was chosen because it has the most samples with the widest range of REE concentrations. Again, the sample with the lowest concentration of REEs (NA101-097) was chosen as the primary melt. This model again produced compositions parallel to the REE data from seamount 2, but only required 5-30% fractional crystallization of 60% CPX, 20% olivine, and 20% plagioclase. This is a more reasonable percentage of fractional crystallization and supports the hypothesis that the range in REE concentrations of seamount 2 can be produced by fractional crystallization of a single parent magma.

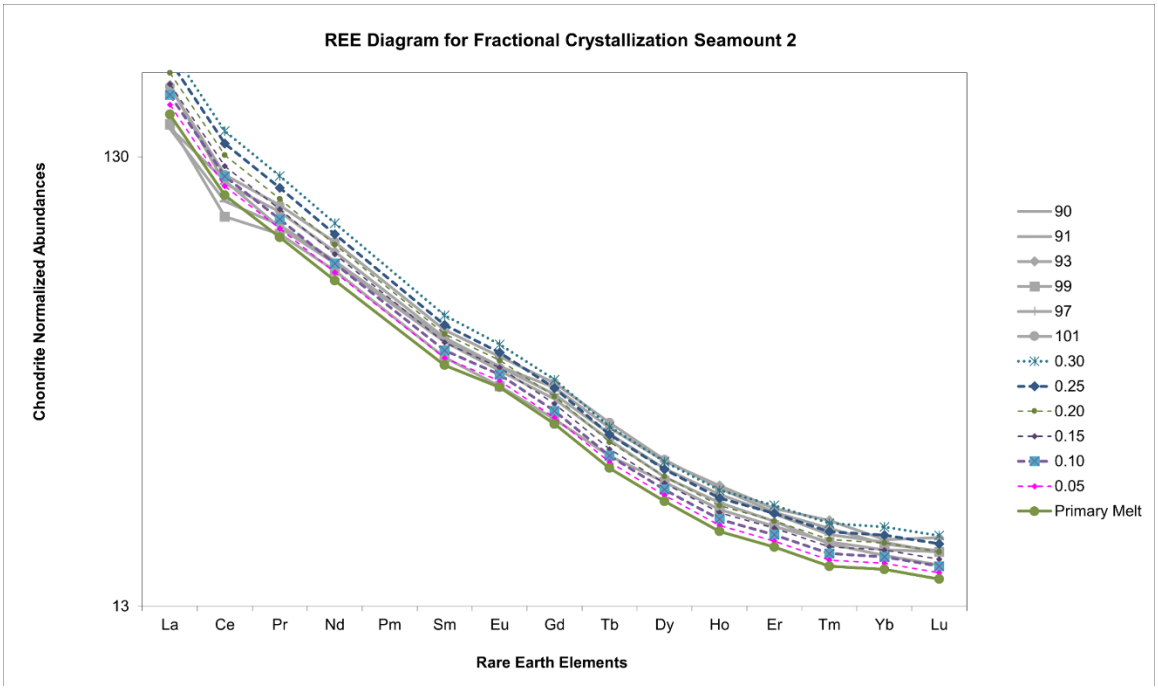

Figure 20. REE fractional crystallization model for samples from seamount 2 using sample NA101-097 as the primary melt. Fractional melts from 5-30% crystallization are shown by colored lines, Naifeh and Plumeria data represented by gray lines.

Mantle Melting

The variation in chemical composition (Figures 13 & 14) is likely partially due to fractional crystallization of CPX from multiple parent magmas as described above. However, variations in extent of partial melting can also affect trace element concentration and ratios in a magma. Here, we use a numerical mantle melting model to both constrain the mantle source and extent of melting required to produce the Naifeh and Plumeria lavas (Figure 21). This will provide a better understanding of the chemical heterogeneity present in these lavas.

A melting model was used to constrain the source and extent of melting required to produce the Naifeh and Plumeria lavas (Figure 21). Melting was calculated using bulk instantaneous fractional melting equation: $C_l = C^o_l * ((1-((1-F)^{(1/D)}))/F)$. D is the bulk distribution coefficient for each element, calculated from the partition coefficients of each element and the modal abundances of minerals in the melt. F is the fraction of melt remaining. C^o_l is the initial concentration of an element in the mantle, and C_l is the concentration of an element in the melt. This equation can be used to determine the concentration of each element in a melt at varying fractions of melting (F), different starting compositions (C^o_l), and varying modal abundances of minerals. Naifeh and Plumeria have REE compositions most similar to OIB and E-MORB (Figure 5), so varying proportions of OIB, DMM and E-MORB from Donnely et al. (2004) were used as a starting composition. The proportion of the three sources were varied in 10% increments from 0 to 100 percent. Melting beneath intraplate ocean islands begins at the garnet peridotite facies (Niu et al., 2011), so mineral modal abundance from garnet

peridotite was used. Modal abundances of minerals were changed until a best fit was achieved. Each starting composition was melted at increments of 1, 2, 5, 10, 15, and 20%.

The melting model that produced a best fit to Naifeh and Plumeria incompatible trace elements used mineral modal proportions of 7% CPX, 2% Garnet, 60% Olivine, 25% OPX, and 6% Plagioclase. The best source was melting a mantle composed of 80% OIB, 10% DMM, and 10% E-MORB (Figure 21). Results of melting this starting composition at 1, 2, 5, 10, 15 and 20% melting are shown (Figure 21).

Increased partial melting lowers the concentration of the more incompatible trace elements more than the less incompatible elements (Figure 21). The trace element patterns from Naifeh and Plumeria are generally parallel (Figures 5, 6, 21) and thus, the difference between the samples with the highest and lowest enrichment in trace elements may be due to fractional crystallization and not partial melting. 5% melting appears to be the best fit to the average seamount composition (although this was not determined statistically). The main result of this modeling is that a mantle source composed of 80/10/10 mix of OIB, DMM and E-MORB with a peridotite bulk composition can account for the average seamount trace element composition. The “best-fit” model presented does not account for the lowest HREE in the seamount lavas. This may result from not having enough garnet in the starting modal compositions or from the bulk distribution coefficients, as HREE are compatible in garnet during melting (Winter, 2010). The source of these seamounts will be discussed further in the following sections by comparing their chemical compositions to other well studied seamounts in the Pacific.

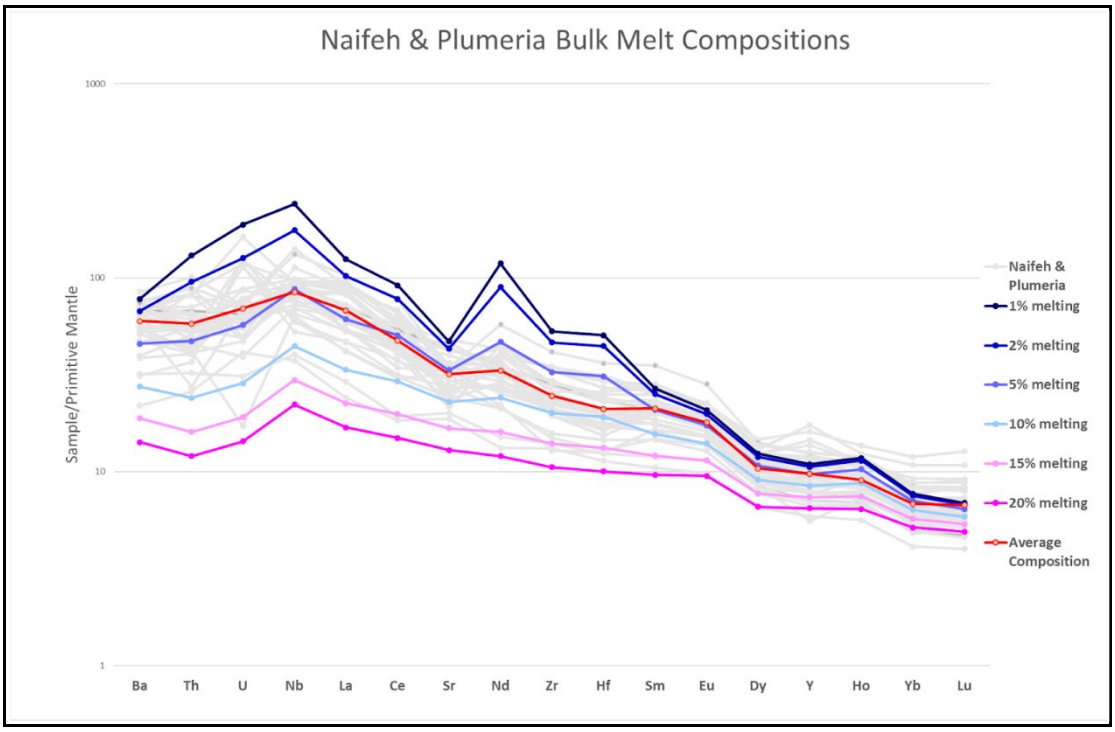

Figure 21. Fractional melting model of trace element patterns using 80% OIB source, 10% DMM and 10% E-MORB Source (Donnely et al., 2004) with crystallization of 7% CPX, 2% Garnet, 60% Olivine, 25% OPX, and 6% Plagioclase. Samples from Naifeh and Plumeria are plotted in grey, excluding altered samples. All values are normalized to the primitive mantle (Sun and McDonough, 1989).

Local Comparisons

The location and orientation of the Naifeh and Plumeria seamount clusters allow for several hypotheses about their origin. The two chains are situated on the Hawaiian arch, so it is possible they are related to arch volcanism and may be similar in composition to the North and South Arch (Frey et al., 2000). They are located at the end of the Murray Fracture Zone, indicating that they may be related to some extensional and deformation related volcanism similar to the Musician Seamounts (O'Connor et al., 2015). They are only ~200 km from the Gardner Pinnacles, the subaerial remnants of the largest shield volcano on earth (Garcia et al., 2020), so comparing them to the NWHR will test whether they are related to off axis upwelling of the Hawaiian plume. The

seamounts could also be formed by widespread cretaceous hotspot volcanism. Here, I compare the Naifeh and Plumeria seamounts compositions to these proximal volcanic features (<200km) to investigate their origins. These include the Musicians seamounts, Northwest Hawaiian Ridge (NWHR), and North Arch seamounts (Figure 1). Other regional datasets (>200km) are investigated in the next section.

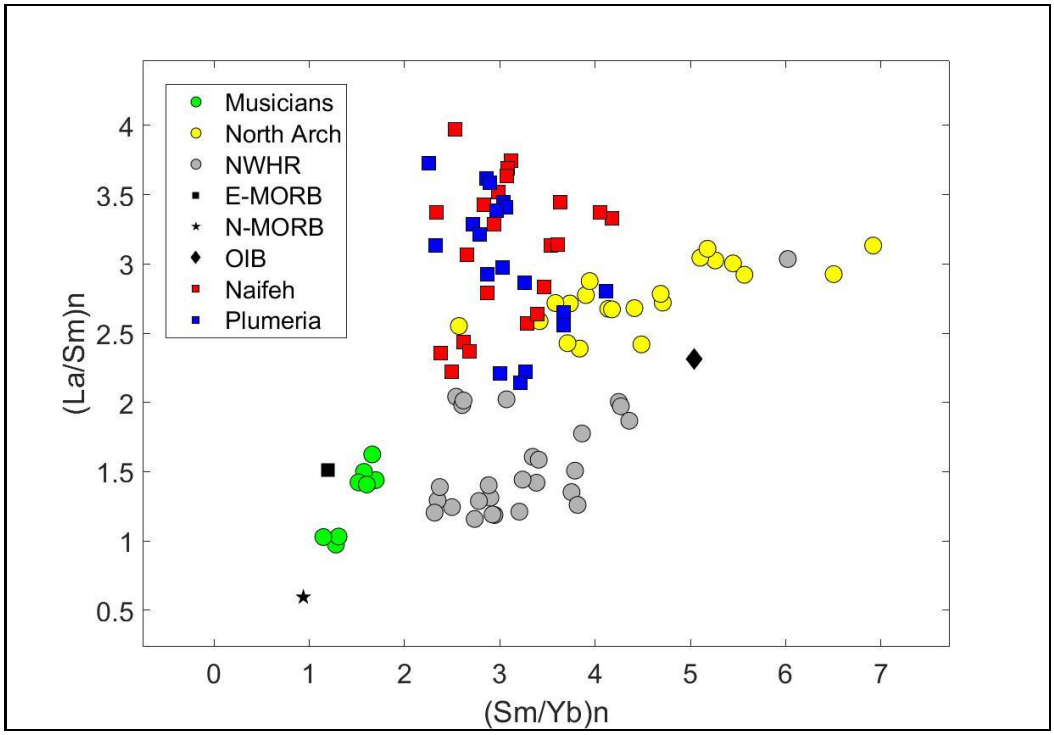

Figure 22. REE ratio comparisons between the Musicians (O'Connor et al., 2015), North Arch (Frey et al., 2000), NWHR (Garcia et al., 2015), and Naifeh and Plumeria (This study). Average values of E-MORB, N-MORB, and OIB from Sun & Mcdonough 1989.

Rare earth element ratios and lead isotope ratios from Cunningham et al., (2019) are used to compare the Naifeh and Plumeria lavas to these nearby volcanic features (Figures 22 and 23). The Musician lavas from O'Connor et al. (2015) are thought to originate from extension and tap a depleted upper mantle source like MORB. The Musician seamount data from O'Connor et al. (2015) only include 50 ma lavas from

reactivated volcanism and not seamounts from the Euterpe hotspot. Isotopic data and trace element ratios from these “young” Musician seamounts are distinct from the Naifeh and Plumeria lavas (Figures 22 and 23). The Euterpe hotspot was active from 96ma to 65ma and erupted near the Pacific Farallon ridge (Pringle, 1992). The Naifeh and Plumeria Seamounts erupted at the same time as the Euterpe hotspot at 80-90ma (Sotomayor et al., 2022). The Musicians seamount lead isotope data from the Euterpe hotspot lavas are closer in isotope ratios than the younger Musicians seamounts (Figure 23), but not they do not overlap, indicating a different mantle source. Their trace element ratios (La/Sm and Sm/Yb) are also lower when compared to Naifeh and Plumeria lavas. No REE data is available for the older Musicians seamounts. Combined, these results suggest that it is not likely that Naifeh and Plumeria were formed by similar extension and deformation related volcanism that taps a depleted upper mantle source or by a source similar to the Euterpe hotspot.

Naifeh and Plumeria have been dated to the late Cretaceous (Sotomayor et al., 2022), which is older than the NWHR, so their formation is not synchronous with any Hawaiian plume related volcanism. This is consistent with the fact that compositions of Naifeh and Plumeria are not like any Hawaiian plume related volcanism. The Naifeh and Plumeria light to middle REE ratios La/Sm in the seamount clusters are much higher than NWHR lavas (Figure 22) and lead isotopes are more enriched (Figure 23). Thus, we concluded that they are unrelated to Hawaiian hotspot volcanism.

The age of Naifeh and Plumeria also suggest that they are not formed from Hawaiian arch volcanism. North and South arch volcanism produces lavas with depleted MORB-like Pb isotopes (Figure 23), and depleted trace elements. Naifeh and Plumeria

are too enriched in Pb isotopes and REEs to have originated from a similar source. Ruling out these three local sources confirms the Naifeh and Plumeria seamounts are not likely formed by arch volcanism, plate deformation and melting that taps a depleted mantle, the Euterpe hotspot, or Hawaiian volcanism. Thus, I broaden my scope to make comparisons with other seamounts in the South Pacific.

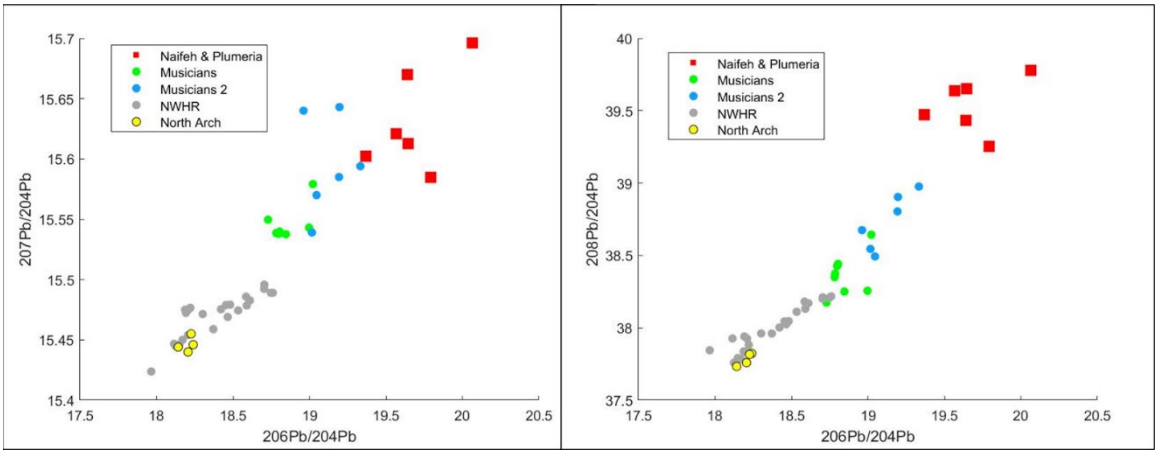

Figure 23. Lead isotope ratios for Naifeh and Plumeria (Cunningham et al., 2019) compared to local volcanic features. Musicians data from O'Connor et al., 2015, Musicians 2 (Pringle, 1992), North Arch (Frey et al., 2000), and NWHR (Harrison et al., 2017).

Regional Comparisons

Many isotopically enriched lavas have been attributed to the South Pacific Isotopic and Thermal Anomaly (SOPITA) (Figure 1), which is a broad region of relatively thin and hot oceanic lithosphere and a high concentration of volcanism (Koppers et al., 2003, McNutt and Fischer, 1987; McNutt and Judge, 1990; Larson, 1991; Cazenave and Thoraval, 1994; McNutt et al., 1996, 1997; McNutt, 1998). The SOPITA region, also known as the "South Pacific Superswell" is characterized by a negative geoid anomaly, shallow seafloor, slow mantle seismic velocities which are attributed to a "Superplume" in the south Pacific mantle (Adam et al., 2014; Staudigel et al., 1991;

Castillo, 1988; McNutt, 1998). The enriched compositions of lavas erupted from this region are explained by incorporation of ancient, recycled crust into the melt (Hanyu et al., 2011). In this section, the Naifeh and Plumeria seamount lavas will be compared to lavas from the SOPITA region, as well as lavas from to the Shatsky and Hess Rises, and the Ojin Rise; seamounts erupted ~1000km to the west of Naifeh and Plumeria (Figure 1) during the early to mid-Cretaceous (Tejada et al., 2016; Dürkefälden et al., 2021). Studies that investigate mantle sources for SOPITA suggest HIMU and EM2 as endmembers (Staudigel et al., 1991). The Pb isotope ratios from Naifeh and Plumeria lavas are similar to FOZO with one sample trending toward HIMU (Figure 22). Sr isotope data is not yet available for Naifeh and Plumeria, but comparing Pb data along with REE patterns will provide a good comparison of melting source to lavas from the SOPITA region.

When compared to a range of datasets from the Pacific, the Naifeh and Plumeria Pb isotope and trace element ratios are most similar to the Line Islands (Figures 24, 27). The Line Islands are Cretaceous seamounts ~800 km south of Naifeh and Plumeria chains. Their origin is disputed, but they are hypothesized to be sourced from multiple hotspots from the SOPITA region (Pockalny et al., 2021) or by small scale sublithospheric convection (SSC) (Ballmer et al., 2007). SSC is a convection in the upper mantle originating from instabilities in the cold dense thermal boundary layer at the bottom of the oceanic lithosphere (Ballmer et al., 2010). Convective upwelling aligned with plate motion causes decompression melting (Ballmer et al., 2010). This type of melting is predicted for non-age-progressive seamount chains like the Line Islands. Many samples from the Line Islands have higher mid to heavy REE ratios than the Naifeh and Plumeria seamounts. This could be due to heterogeneity in the upper mantle or

differences in degrees of partial melting. Even with these slight differences, there is still considerable overlap between the Line Islands and Naifeh and Plumeria (Figure 24, 25), suggesting that they could be formed by similar volcanic processes.

There is also overlap in REEs with lavas from Rurutu, an island in the Austral-Cook seamount chain. Isotopes from Rurutu are more radiogenic and trend towards a more HIMU-like source. Only one sample overlaps with the Rurutu data in Pb isotope space sample Na101-104 from Plumeria (Figures 24 & 27). However, this sample was removed from our trace element dataset due to significant alteration. Thus, this may indicate this sample originated from a different source that is more similar to Rurutu or the Pb isotopes are affected by alteration as well. Rurutu is hypothesized to form from either the long lived (Hanyu et al., 2011; Hanyu et al., 2013) MacDonald hotspot, originating within the SOPITA region of the mantle or from small scale sublithospheric convection (Ballmer et al., 2007).

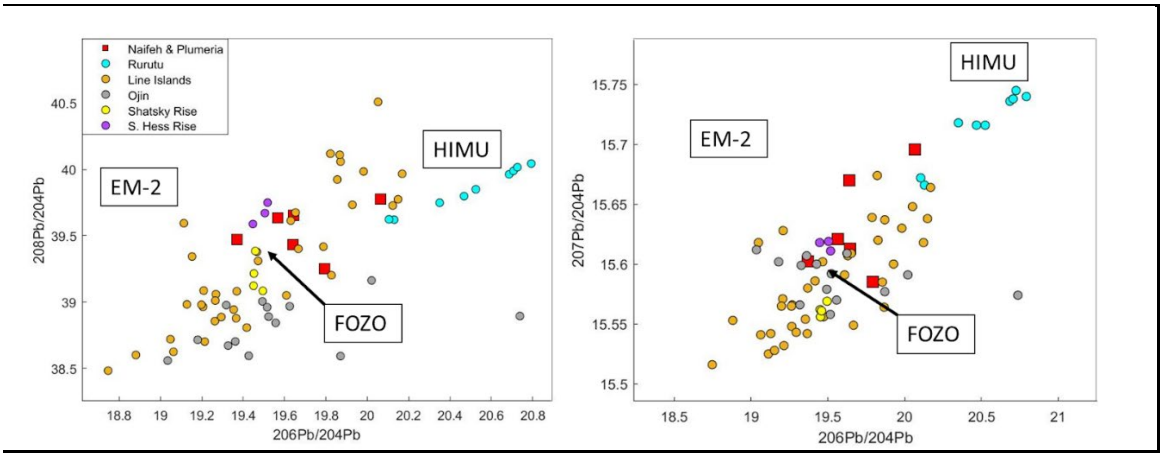

Figure 24. Pb isotope data for Naifeh and Plumeria (Cunningham et al., 2019), Rurutu (Hanyu et al., 2013), Line Islands (Garcia et al., 1993; Storm, 2012), Ojin seamounts (Sano et al., 2020), Shatsky Rise, and Southern Hess Rise seamounts (Tejada et al., 2016).

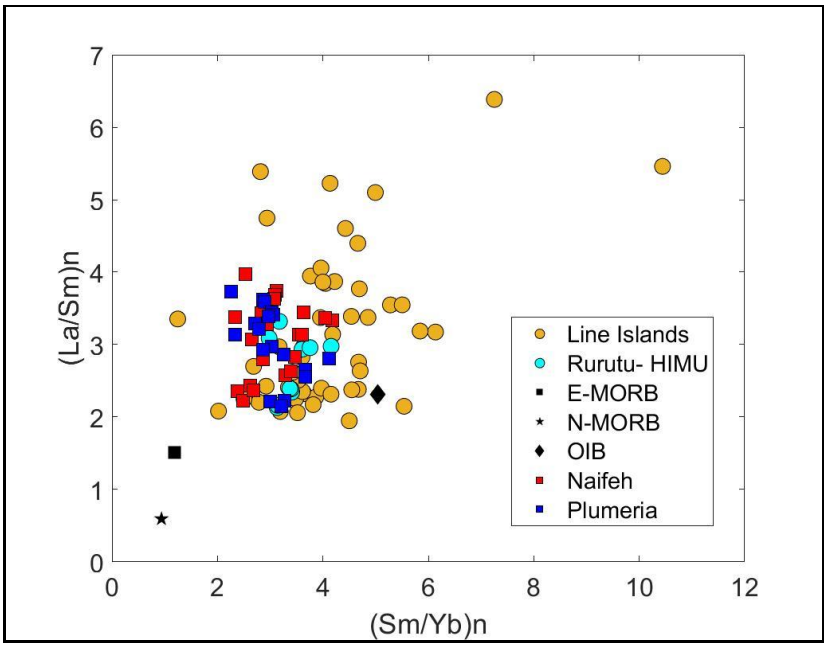

Figure 25. REE ratio comparison between Naifeh and Plumeria lavas with isotope data, and Rurutu (Hanyu et al., 2013), and Line Islands (Davis et al., 2002).

The seamount samples are also isotopically similar to lavas from the Ojin Seamounts, Shatsky Rise and Southern Hess Rise (Figure 24). Shatsky Rise and Southern Hess Rise are similar to FOZO (Figure 24), while Ojin is slightly less radiogenic. The Ojin seamounts, Southern Hess Rise, and Shatsky Rise lavas have lower Sm/Yb ratios than the 5 Naifeh and Plumeria samples that were analyzed for lead isotopes (Figure 26). Many samples from Naifeh and Plumeria have lower Sm/Yb ratios, but currently have no isotope data (Figure 23). If lower Sm/Yb samples from Naifeh and Plumeria are also less radiogenic, they may have a similar source as the Shatsky and Hess rises, as well as the Ojin Rise seamounts.

The Shatsky Rise, Ojin Rise, and Hess Rise seamounts have been predicted to be from the same hotspot source, which erupted near the Pacific-Farallon-Izanagi triple junction during the early Cretaceous (Dürkefälden et al., 2021; Tejada et al., 2016; Torsvik et al., 2019). Crude plate reconstructions suggest that the source of Naifeh and

Plumeria is likely near the Pacific Farallon ridge, so it is possible the sources of Shatsky, Hess, and Ojin are similar. If this hotspot continued erupting through the mid-cretaceous, its track may continue through the Liliuokalani seamount chain (Figure 2) and intersect with the Naifeh and Plumeria chains. Thus, it is possible all these seamounts are from the same hotspot; however, isotope and age data from the Liliuokalani seamounts is needed to confirm this hypothesis, as well as detailed plate reconstruction to track the source of these hotspots.

It is clear from these rare earth element ratio and lead isotope comparisons that the Naifeh and Plumeria chemical compositions are similar to several hotspot related volcanic chains either emanating from the SOPITA region or from small-scale sublithospheric convection, similar to Rurutu and the Line Islands. Since the geochemical signatures are similar, more age data is necessary to make the distinction between these two hypotheses. For example, a volcanic hotspot would likely have age progressive volcanism, while small scale convection should not be age progressive.

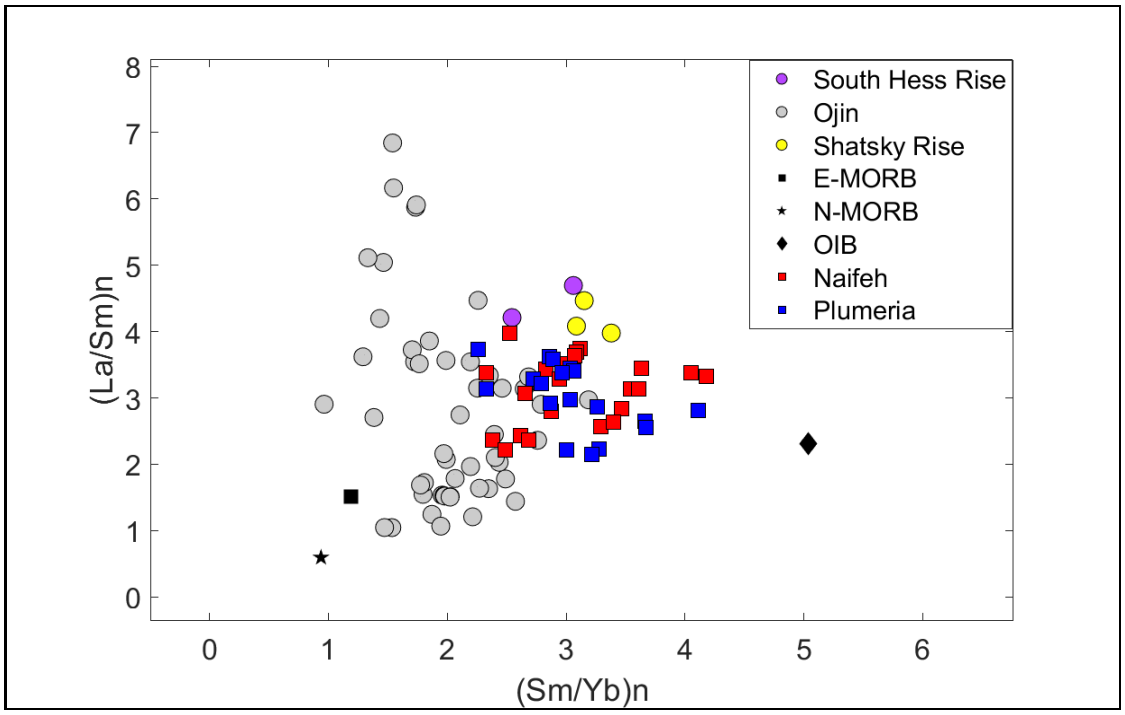

Figure 26. REE ratio data for Naifeh and Plumeria, Ojin Rise seamounts (Dürkefälden et al., 2021), Southern Hess Rise, and Shatsky Rise (Tejada et al., 2016).

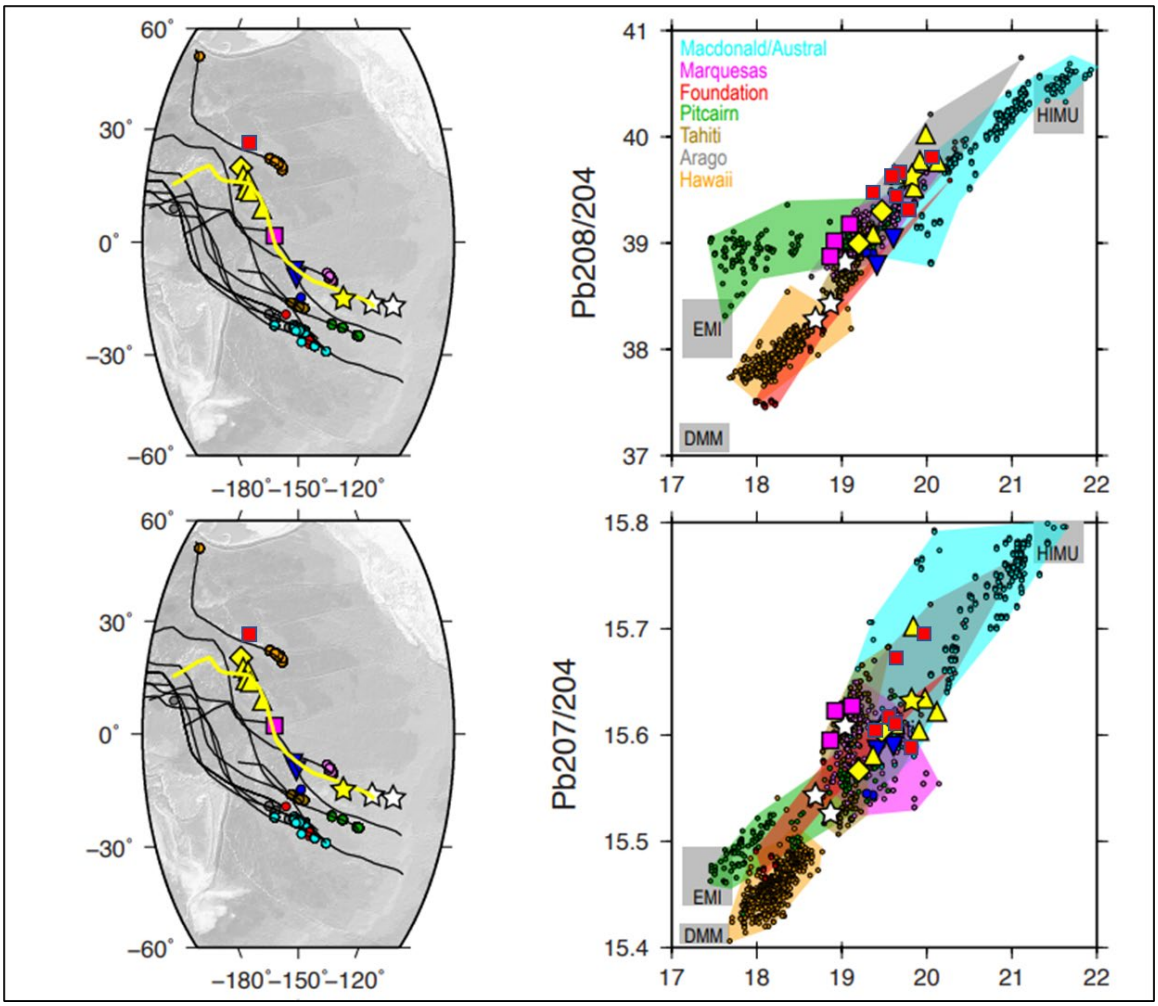

Figure 27. Modified from Pockalny, 2021. Red squares are Pb isotope data from Naifeh and Plumeria (Cunningham et al., 2019).

Causes of enigmatic orientation

Another outstanding question is the enigmatic orientation of the Naifeh and Plumeria chains. Figure 1 shows the chains are parallel to the Hawaiian seamounts, but hotspot chains of similar age (~86ma) have orientations that are NW-SE trending (eg. Line Islands, Wentworth & Musician chains). Here, I will provide some possible scenarios for the orientation of the Naifeh and Plumeria chains.

Although age dates are limited to only 2 samples, the Naifeh and Plumeria seamount lavas are dated to ~86ma (Sotomayor et al., 2022). The orientation Naifeh and

Plumeria seamounts chains follow the alignment of the 0-43ma northwest Hawaiian ridge. (Figure 1). This orientation is not typical of other Cretaceous aged seamount chains. Plate reconstructions from Pockalny et al. (2021) of the Line Island chains show a bend in the hotspot trails from 80-100ma (Figure 28). The Naifeh and Plumeria chains could be at the apex of this bend, erupting at a period of plate motion change. If the hotspot follows the same trajectory of the Line Islands hotspot, any seamounts older than Naifeh and Plumeria would have been overlain by the younger Hawaiian seamounts. Following the hotspot trail from Pockalny et al. (2021) to the east would put the source of the hotspot east of the Marquesas Islands (Figure 28), within the SOPITA region. This could account for the enriched isotopes of the Naifeh and Plumeria seamounts. There is no evidence that a hotspot at this location produced any large seamounts from 0-80ma; after eruption of seamounts from this study. Plate reconstructions from Pringle (1992) traces the Musician seamounts near the Pacific Farallon ridge ~70-95ma, erupting near the equator. This would also put the Naifeh and Plumeria seamounts near the equator, erupting ~200km southwest of the Musicians hotspot source during the Cretaceous. It is also possible the Naifeh and Plumeria chains are a continuation of the Liliuokalani chain or Wentworth chain to the west, but geochemical data from these regions would need to be collected to confirm this.

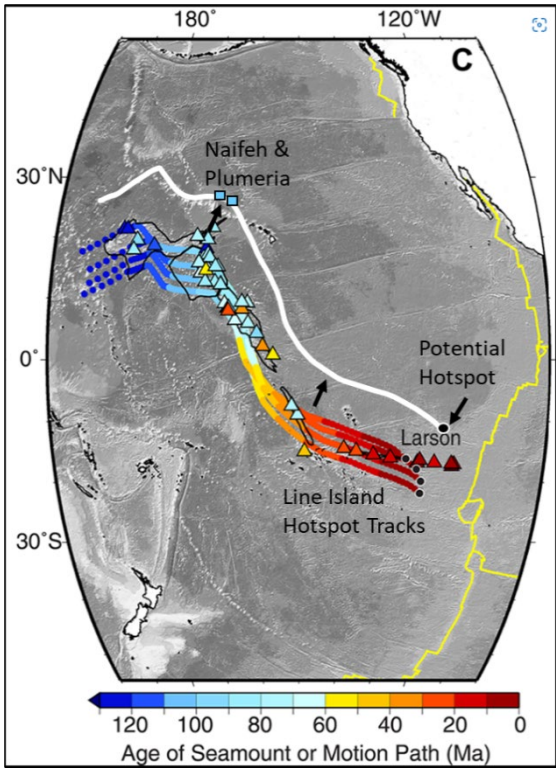

Figure 28 Potential hotspot track (white) for the Naifeh and Plumeria seamounts translated from line islands hot spot tracks by Pockalny et al. (2021).

CONCLUSIONS

Major and trace element analysis of the Naifeh and Plumeria seamount clusters reveal the lavas are alkalic trachybasalts to trachyandesites, with low MgO concentrations (2.82-0.89 wt.%) and enriched trace element concentrations compared to MORB. The rare earth element ratios of the two clusters have the same median values, and isotopic data suggest they are from the same mantle source. The Naifeh cluster has the same rare earth element ratios and similar REE patterns as Plumeria, but have slightly higher concentrations of rare earth elements, perhaps due to higher relative degrees of fractional crystallization. Modeling fractional crystallization using Petrolog3 showed some of the lavas from Naifeh and Plumeria are related through the fractional crystallization of clinopyroxene, but multiple parent lavas are required to account for all of the data. A fractional melting model constrained the mantle source to be 80% OIB, 10% EMORB and 10% DMM, with mineral modal proportions of 7% CPX, 2% garnet, 60% olivine, 25% OPX, and 6% plagioclase. Although more sophisticated melting models would better constrain this.

Naifeh and Plumeria are ~86ma and have no isotopic or trace element similarities to the Musician seamounts, northwest Hawaiian ridge, or North Arch seamounts. This rules out deformation related volcanism, off-axis Hawaiian volcanism and arch volcanism, respectively, as mechanisms of formation. The Naifeh and Plumeria seamounts may have erupted from hotspot volcanism stemming from the SOPITA region of the south Pacific or by sublithospheric convection that taps an enriched mantle. Their

FOZO lead isotope signatures and rare earth element ratios are most similar to the Line Island and Rurutu seamounts. Rare earth element ratios and isotopes are most like the Line islands and Rurutu, but also have some overlap with the Shatsky Rise, Southern Hess rise and Ojin seamounts, which are also products of hotspot volcanism from the SOPITA region. The Naifeh and Plumeria seamounts do not trend with hotspot chains of similar age. A hotspot track reconstruction (Figure 26) puts the two clusters at a bend in plate motion and their potential hotspot within the SOPITA region. More age data is needed to fully understand the eruptive mechanism of these seamounts, whether they formed via hotspot or sublithospheric convection.

REFERENCES

Adam, C., Yoshida, M., Suetsugu, D., Fukao, Y., & Cadio, C. (2014). Geodynamic modeling of the South Pacific superswell. *Physics of the Earth and Planetary Interiors*, *229*, 24–39. https://doi.org/10.1016/j.pepi.2013.12.014

Ballmer, M. D., Ito, G., van Hunen, J., & Tackley, P. J. (2010). Small-scale sublithospheric convection reconciles geochemistry and geochronology of "Superplume" volcanism in the western and south Pacific. *Earth and Planetary Science Letters*, 290(1–2), 224–232. https://doi.org/10.1016/j.epsl.2009.12.025

Ballmer, M. D., van Hunen, J., Ito, G., Tackley, P. J., and Bianco, T. A. (2007), Non-hotspot volcano chains originating from small-scale sublithospheric convection, *Geophys. Res. Lett.,* 34, L23310, https://doi.org/10.1029/2007GL031636.

Bellot, N., Boyet, M., Doucelance, R., Bonnand, P., Savov, I. P., Plank, T., & Elliott, T. (2018). Origin of negative cerium anomalies in subduction-related volcanic samples: Constraints from Ce and Nd isotopes. *Chemical Geology*, 500, 46–63. https://doi.org/10.1016/J.CHEMGEO.2018.09.006

Bianco, T. A., Ito, G., Becker, J. M., & Garcia, M. O. (2005). Secondary Hawaiian volcanism formed by flexural arch decompression. *Geochemistry, Geophysics, Geosystems*, *6*(8), 1–24. https://doi.org/10.1029/2005GC000945

Bulmer, M. H., & Wilson, J. B. (1999). Comparison of flat-topped stellate seamounts on Earth's seafloor with stellate domes on Venus using side-scan sonar and Magellan synthetic aperture radar. Earth and Planetary Science Letters, 171(2), 277–287. https://doi.org/https://doi.org/10.1016/S0012-821X(99)00154-5

Castillo, P. (1988). The Dupal anomaly as a trace of the upwelling lower mantle. *Nature*, 336(6200), 667–670. https://doi.org/10.1038/336667a0

Cazenave, A., & Thoraval, C. (1994). Mantle dynamics constrained by degree 6 surface topography, seismic tomography and geoid: Inference on the origin of the South Pacific Superswell. *Earth and Planetary Science Letters*, 122(1), 207–219. https://doi.org/10.1016/0012-821X(94)90061-2

Cunningham, M., Konter, J., Wanless, V. D., Balbas, A., (2019), Enigmatic Seamounts: Investigating Pacific Intraplate Volcanism with Lead Isotopes, Abstract [V43H-0184] presented at 2019 Fall Meeting, AGU, San Francisco, CA, 9-13 Dec.

Danyushevsky, L. V., and Plechov, P. (2011), Petrolog3: Integrated software for modeling crystallization processes, *Geochem. Geophys. Geosyst*., 12, Q07021, https://doi.org/10.1029/2011GC003516.

Davis, A. S., Gray, L. B., Clague, D. A., & Hein, J. R. (2002). The Line Islands revisited: New 40Ar/39Ar geochronologic evidence for episodes of volcanism due to lithospheric extension. *Geochemistry, Geophysics, Geosystems*, 3(3), 1–28. https://doi.org/10.1029/2001GC000190

Donnelly, Kathleen & Goldstein, Steven & Langmuir, Charles & Spiegelman, Marc. (2004). Origin of enriched ocean ridge basalts and implications for mantle dynamics. *Earth and Planetary Science Letters*. 226. 347-366. https://doi.org/10.1016/j.epsl.2004.07.019.

Dürkefälden, A., Geldmacher, J., Portnyagin, M., Garbe-Schönberg, D., Werner, R., Müller, D., et al. (2021). Papanin Ridge and Ojin Rise Seamounts (Northwest Pacific): Dual hotspot tracks formed by the Shatsky plume. *Geochemistry, Geophysics, Geosystems,* 22, e2021GC009847. https://doi.org/10.1029/2021GC009847

Frey, F. A., Clague, D., Mahoney, J. J., & Sinton, J. M. (2000). Volcanism at the Edge of the Hawaiian Plume: Petrogenesis of Submarine Alkalic Lavas from the North Arch Volcanic Field. *Journal of Petrology*, 41(5), 667–691. https://doi.org/10.1093/petrology/41.5.667

Garcia, M. O., Park, K.-H., Davis, G. T., Staudigel, H., & Mattey, D. P. (1993). Petrology and Isotope Geochemistry of Lavas from the Line Islands Chain, Central Pacific Basin. *In The Mesozoic Pacific: Geology, Tectonics, and Volcanism* (pp. 217–231). https://doi.org/10.1029/GM077p0217

Garcia, M. O., Smith, J. R., Tree, J. P., Weis, D., Harrison, L., & Jicha, B. R. (2015). Nick Bulloss. In C. R. Neal, W. W. Sager, T. Sano, & E. Erba (Eds.), The Origin, Evolution, and Environmental Impact of Oceanic Large Igneous Provinces (Vol. 511, p. 0). *Geological Society of America*. https://doi.org/10.1130/2015.2511(01)

Garcia, M. O, Swinnard, L., Weis, D., Greene, A., Tagami, T., Sano, H., & Gandy, C. (2010). Petrology, Geochemistry and Geochronology of Kaua'i Lavas over 4.5 Myr: Implications for the Origin of Rejuvenated Volcanism and the Evolution of the Hawaiian Plume. *Journal of Petrology*, 51, 1507–1540. https://doi.org/10.1093/petrology/egq027

Garcia, M. O, Tree, J., Wessel, P., & Smith, J. (2020). Pūhāhonu: Earth's biggest and hottest shield volcano. *Earth and Planetary Science Letters*, 542, 116296. https://doi.org/10.1016/j.epsl.2020.116296

Hanyu, T., Dosso, L., Ishizuka, O., Tani, K., Hanan, B. B., Adam, C., Nakai, S., Senda, R., Chang, Q., & Tatsumi, Y. (2013). Geochemical diversity in submarine HIMU basalts from Austral Islands, French Polynesia. *Contributions to Mineralogy and Petrology*, 166(5), 1285–1304. https://doi.org/10.1007/s00410-013-0926-x

Hanyu, T., Tatsumi, Y., Senda, R., Miyazaki, T., Chang, Q., Hirahara, Y., Takahashi, T., Kawabata, H., Suzuki, K., Kimura, J.-I., & Nakai, S. (2011). Geochemical characteristics and origin of the HIMU reservoir: A possible mantle plume source in the lower mantle. *Geochemistry, Geophysics, Geosystems*, 12(2). https://doi.org/10.1029/2010GC003252

Harrison, L. N., Weis, D., & Garcia, M. O. (2017). The link between Hawaiian mantle plume composition, magmatic flux, and deep mantle geodynamics. *Earth and Planetary Science Letters*, 463, 298–309. https://doi.org/10.1016/j.epsl.2017.01.027

Hart, S. R., & Staudigel, H. (1982). The control of alkalies and uranium in seawater by ocean crust alteration. *Earth and Planetary Science Letters*, 58(2), 202–212. https://doi.org/10.1016/0012-821X(82)90194-7

Hofmann, A. W., & White, W. M. (1982). Mantle plumes from ancient oceanic crust. *Earth and Planetary Science Letters*, 57(2), 421–436. https://doi.org/10.1016/0012821X(82)901613

Hunt, J. E., & Jarvis, I. (2020). The lifecycle of mid-ocean ridge seamounts and their prodigious flank collapses. *Earth and Planetary Science Letters*, 530, 115867. https://doi.org/10.1016/j.epsl.2019.115867

Kelley, K. A., Plank, T., Ludden, J., & Staudigel, H. (2003). Composition of altered oceanic crust at ODP Sites 801 and 1149. *Geochemistry, Geophysics, Geosystems*, 4(6). https://doi.org/10.1029/2002GC000435

Koppers, A. A. P., Staudigel, H., Pringle, M. S., & Wijbrans, J. R. (2003). Short-lived and discontinuous intraplate volcanism in the South Pacific: Hot spots or extensional volcanism? *Geochemistry, Geophysics, Geosystems,* 4(10). https://doi.org/10.1029/2003GC000533

Larson, R. L. (1991). Geological consequences of superplumes. *Geology*, 19(10), 963–966. https://doi.org/10.1130/0091-7613(1991)019<0963:GCOS>2.3.CO;2

Le Maitre, R.W., Bateman, P., Dudek, A.J. and Keller, M.J. (1989) A Classification of Igneous Rocks and Glossary of Terms, Blackwell, Oxford, 193.

Lipman, P. W., Clague, D. A., Moore, J. G., & Holcomb, R. T. (1989). South Arch volcanic field - Newly identified young lava flows on the sea floor south of the Hawaiian Ridge. *Geology,* 17(7), 611–614. https://doi.org/10.1130/0091-7613(1989)017<0611:SAVFNI>2.3.CO;2

Lytle, M. L., Kelley, K. A., Hauri, E. H., Gill, J. B., Papia, D., & Arculus, R. J. (2012). Tracing mantle sources and Samoan influence in the northwestern Lau back-arc basin. *Geochemistry, Geophysics, Geosystems,* 13(10). https://doi.org/10.1029/2012GC004233

MacDonald, G.A. and Katsura, T. (1964). Chemical Composition of Hawaiian Lavas. *Journal of Petrology*, 5(1), 82-133. https://doi.org/10.1093/petrology/5.1.82

McDonough, W. F., Sun, S.-S., Ringwood, A. E., Jagoutz, E., & Hofmann, A. W. (1992). Potassium, rubidium, and cesium in the Earth and Moon and the evolution of the mantle of the Earth. *Geochimica et Cosmochimica Acta*, 56(3), 1001–1012. https://doi.org/10.1016/0016-7037(92)90043-I

McDonough, W. F., & Sun, S. -S.,(1995). The composition of the Earth. *Chemical Geology*, 120(3), 223–253. https://doi.org/10.1016/0009-2541(94)00140-4

McNutt, M. K. (1998). Superswells. *Reviews of Geophysics*, 36(2), 211–244. https://doi.org/10.1029/98RG00255

Mcnutt, M.K. and Fischer, K.M. (1987). The South Pacific Superswell. In Seamounts, Islands, and Atolls (eds B.H. Keating, P. Fryer, R. Batiza and G.W. Boehlert). https://doi.org/10.1029/GM043p0025

McNutt, M. K., & Judge, A. v. (1990). The Superswell and Mantle Dynamics Beneath the South Pacific. *Science,* 248(4958), 969–975. https://doi.org/10.1126/science.248.4958.969

McNutt, M. K., Sichoix, L., & Bonneville, A. (1996). Modal depths from shipboard bathymetry: There is a south pacific superswell. *Geophysical Research Letters*, 23(23), 3397–3400. https://doi.org/10.1029/96GL03053

McNutt, M. K., Caress, D. W., Reynolds, J., Jordahl, K. A., & Duncan, R. A. (1997). Failure of plume theory to explain midplate volcanism in the southern Austral islands. *Nature*, 389(6650), 479–482. https://doi.org/10.1038/39013

Morgan, W. J. (1971). Convection Plumes in the Lower Mantle. *Nature*, 230(5288), 42–43. https://doi.org/10.1038/230042a0

Niu, Y., Wilson, M., Humphreys, E. R., & O'Hara, M. J. (2011). The Origin of Intra-plate Ocean Island Basalts (OIB): the Lid Effect and its Geodynamic Implications. *Journal of Petrology*, 52(7–8), 1443–1468. https://doi.org/10.1093/petrology/egr030

O'Connor, J. M., Hoernle, K., Dietmar Müller, R., Morgan, J. P., Butterworth, N. P., Hauff, F., Sandwell, D. T., Jokat, W., Wijbrans, J. R., & Stoffers, P. (2015). Deformation-related volcanism in the Pacific Ocean linked to the Hawaiian-Emperor bend. *Nature Geoscience*, *8*(5), 393–397. https://doi.org/10.1038/ngeo2416

Pockalny, R., Barth, G., Eakins, B., Kelley, K. A., & Wertman, C. (2021). Multiple melt source origin of the Line Islands (Pacific Ocean). *Geology*, 49(11), 1358–1362. https://doi.org/10.1130/G49306.1

Pringle, M. S. (1992). Geochronology and petrology of the Musicians seamounts, and the search of hotspot volcanism in the Cretaceous Pacific, Ph.D. Thesis, Univ. of Hawaii, Honolulu.

Richards, F. D., Kalnins, L. M., Watts, A. B., Cohen, B. E., & Beaman, R. J. (2018). The morphology of the Tasmantid Seamounts: Interactions between tectonic inheritance and magmatic evolution. *Geochemistry, Geophysics, Geosystems,* 19, 3870– 3891. https://doi.org/10.1029/2018GC007821

Sano, T., Hanyu, T., Tejada, M. L. G., Koppers, A. A. P., Shimizu, S., Miyazaki, T., Chang, Q., Senda, R., Vaglarov, B. S., Ueki, K., Toyama, C., Kimura, J.-I., & Nakanishi, M. (2020). Two-stages of plume tail volcanism formed Ojin Rise Seamounts adjoining Shatsky Rise. *Lithos*, *372–373*, 105652. https://doi.org/10.1016/j.lithos.2020.105652

Schmidt, R., Schmincke, H.-U. (2000). Seamounts and island building. In: Sigurdsson, H., Houghton, B.F., McNutt, S.R., Rymer, H., Stix, J. (Eds.), Encyclopedia of Volcanoes. Academic Press, San Diego and London, pp. 383–402.

Sherrod, D. R., Sinton, J., Watkins, S. E., & Brunt, K. M. (2007). Geologic map of the State of Hawai'i: US. Geological Survey Open-File Report, 1089–2007.

Smith, W., & Sandwell, D. (1997). Global Sea Floor Topography from Satellite Altimetry and Ship Depth Soundings. Science, 277, 1956–1962.

Sotomayor, A., Balbas, A., Konrad, K., Koppers, A.P., Konter, J., Wanless, V.D., Hourigan, T.F., Kelley, C., Raineault, N. (2022). New Insights into the Age and Origin of Two Small Cretaceous Seamount Chains Proximal to the Northwestern Hawaiian Ridge. Accepted to Geosphere.

Staudigel, H., and D.A. Clague. (2010). The geological history of deep-sea volcanoes: Biosphere, hydrosphere, and lithosphere interactions. *Oceanography* 23(1): 58–71, https://doi.org/10.5670/oceanog.2010.62.

Staudigel, H., Park, K.-H., Pringle, M., Rubenstone, J. L., Smith, W. H. F., & Zindler, A. (1991). The longevity of the South Pacific isotopic and thermal anomaly. *Earth and Planetary Science Letters*, *102*(1), 24–44. https://doi.org/10.1016/0012-821X(91)90015-A

Staudigel, H., Plank, T., White, B. and Schmincke, H.-U. (1996). Geochemical Fluxes During Seafloor Alteration of the Basaltic Upper Oceanic Crust: DSDP Sites 417 and 418. In Subduction (eds G.E. Bebout, D.W. Scholl, S.H. Kirby and J.P. Platt). https://doi.org/10.1029/GM096p0019

Storm, L. (2012). Isotope Geochemistry and Geochronology of Lavas from the Line Islands Chain, Central Pacific Basin: Insight into the Origin of the Line Islands. Open Access Theses & Dissertations.
2200. https://scholarworks.utep.edu/open_etd/2200

Sun, S.S. and McDonough, W.F. (1989) Chemical and Isotopic Systematics of Oceanic Basalts: Implications for Mantle Composition and Processes. In: Saunders, A.D., Norry, M.J., Eds., Magmatism in the Ocean Basins, Geological Society, London, Special Publications, 42, 313-345.
https://doi.org/10.1144/GSL.SP.1989.042.01.19

Tejada, M. L. G., Geldmacher, J., Hauff, F., Heaton, D., Koppers, A. A. P., Garbe-Schönberg, D., Hoernle, K., Heydolph, K., & Sager, W. W. (2016). Geochemistry and age of Shatsky, Hess, and Ojin Rise seamounts: Implications for a connection between the Shatsky and Hess Rises. *Geochimica et Cosmochimica Acta*, *185*, 302–327.

Torsvik, T. H., Steinberger, B., Shephard, G. E., Doubrovine, P. V., Gaina, C., Domeier, M., et al. (2019). Pacific-Panthalassic reconstructions: Overview, errata and the way forward. *Geochemistry, Geophysics, Geosystems,* 20(7), 3659-3689. https://doi.org/10.1029/2019gc008402

Weis, D., Garcia, M. O., Rhodes, J. M., Jellinek, M., & Scoates, J. S. (2011). Role of the deep mantle in generating the compositional asymmetry of the Hawaiian mantle plume. *Nature Geoscience,* 4, 831–838 https://doi.org/10.1038/ngeo1328

Wessel, P., Sandwell, D. T., & Kim, S.-S. (2010). The Global Seamount Census. *Oceanography*, *23*(1), 24–33.

White, W. M., and A. W. Hofmann. (1982). Sr and Nd isotope geochemistry of oceanic basalts and mantle evolution, *Nature*, 296, 821– 825.

Wilson, J. T. (1963). A Possible Origin of the Hawaiian Islands. *Canadian Journal of Physic*s, 41(6), 863–870. https://doi.org/10.1139/p63-094

Winter, J. D. (2010). Mantle Melting and the Generation of Basaltic Magma. In An introduction to igneous and Metamorphic Petrology (pp. 183–200). essay, Prentice Hall.

Zindler, A., & Hart, S. (1986). Chemical Geodynamics. *Annual Review of Earth and Planetary Sciences*, 14(1), 493–571. https://doi.org/10.1146/annurev.ea.14.050186.002425

APPENDIX A

Geochemical Data

Table A1. Major Elements and rock type classification of the Naifeh and Plumeria seamounts. Rock types are Basaltic Trachyandesites (BTA), Trachyandesites (TA), and Trachybasalts (TB)

Sample	Seamount	Latitude	Longitude	Rock	SiO2	TiO2	Al2O3	Fe2O3	MnO	MgO	CaO	Na2O	K2O	P2O5	LOI	total	Sr	Zr
NA101-				Type	wt%	wt%	wt%	wt%	wt%	wt%	wt%	wt%	wt%	wt%	%	%	ppm	ppm
004	6	26.7893325	-166.91755	BTA	51.7	2.66	19.1	7.64	0.071	1.23	7.93	4.27	3.3	0.93		98.8	863	318
007	6	26.7885615	-166.9124	BTA	52.18	2.75	20.12	7.6	0.072	1.22	7.05	4.47	2.95	1		99.4	956	324
010	7	26.7865764	-167.36017	BTA	53.8	3.18	19.2	8.48	0.032	1.27	4.66	3.72	4.26	1.08		99.6	522	184
013	7	26.7960174	-167.36652	BTA	52.23	2.68	23.88	4.24	0.063	0.87	8.43	3.77	2.09	1.97	4.19	100	793	205
015	7	26.8011537	-167.36946	BTA	53.78	2.88	20.07	7.31	0.033	1.21	5.32	3.45	3.41	0.82	2.02	98.3	558	171
023	8	26.851858	-168.0658	BTA	54.28	2.01	19.41	7.35	0.115	1.92	6.33	4.66	2.71	1.12		99.9	726	364
024	8	26.852582	-168.06642	TA	54.37	1.96	18.59	7.39	0.144	1.03	5.64	5.17	3.57	1.1		99	613	336
026	8	26.8539595	-168.06793	BTA	49.69	1.89	17.84	7.86	0.151	0.92	8.94	4.71	2.75	4.61		99.4	682	334

030	8	26.8570134	-168.07465	BTA	51.15	2.42	18.26	8.52	0.105	1.8	8.18	3.94	2.7	1.81	1.55	98.9	590	214
035	10	26.9759942	-168.85529	TB	48.8	2.37	19.1	13.58	0.054	1.95	8.87	2.9	2.38	1.4	4.15	102	399	173
043	10	26.9724125	-168.86059	BTA	51.7	2.48	19.5	6.56	0.086	2.14	9.5	4.25	1.63	0.52		98.4	633	186
044	9	27.0338199	-168.49786	BTA	51.5	2.96	19.1	9.42	0.091	0.96	6.51	3.96	3.28	1.64		99.4	557	286
045	9	27.0315355	-168.49604	BTA	51	2.77	18.3	8.42	0.085	1.68	7.49	3.85	3.06	2.57		99.2	538	296
050	9	27.0286544	-168.49443	BTA	50.3	2.57	18.8	10.62	0.112	1.05	6.27	3.68	3.8	1.22		98.4	747	227
063	6	26.71172	-166.9882	BTA	51.6	2.58	19.5	9.26	0.083	1.92	6.66	3.84	2.8	1.67	3.12	99.9	820	234
065	4	25.9717938	-164.74609	TB	49.4	3.34	18.9	10.19	0.075	0.89	8.07	3.68	2.84	1.73	2.24	99.1	589	232
068	4	25.9715975	-164.74467	TB	49.87	3.01	17.6	8.45	0.092	2.82	9.76	3.42	2.36	0.72	2.76	98.1	593	218
071	4	25.9729337	-164.74023	BTA	52.4	2.61	19.7	7.95	0.076	1.45	7.16	3.87	2.98	1.02	1.96	99.2	889	299
074	3	25.5545084	-164.20247	TA	55.01	2.07	20.02	3.04	0.018	0.73	8.25	4.83	2.92	3.01	2.63	99.9	560	359

090	2	25.3984594	-163.91596	BTA	50.57	2.7	20.04	9.77	0.058	0.78	6.4	3.48	3.5	0.8	2.32	98.1	542	209
091	2	25.3984805	-163.91598	BTA	50.45	2.7	19.93	9.43	0.052	0.74	6.71	3.56	3.51	1.09	1.24	98.2	543	208
093	2	25.3991375	-163.91743	TB	49.6	2.6	19.4	9.18	0.071	0.83	8.51	3.42	3.32	1.24	3.36	98.2	541	196
094	2	25.4023655	-163.92354	TB	48.5	2.54	20.4	7.09	0.027	2.04	10.58	3.28	1.91	3.84		100	702	212
097	2	25.402606	-163.92466	BTA	52.3	2.61	19.7	7.92	0.073	1.44	7.13	3.91	2.96	1.02	2.74	99.1	871	296
099	2	25.4033525	-163.92549	TB	48.4	2.72	20.3	8.94	0.068	0.92	8.83	3.56	2.67	2.4		98.9	641	224
102	2	25.4033372	-163.9256	TB	50.1	2.67	20.2	9.17	0.079	1.24	8.08	3.55	2.76	1.19	2.77	99	599	215
113	1	25.3173239	-163.7419	BTA	52.4	3.63	20.5	7.54	0.052	1.97	7.21	3.33	2.26	0.67	3.48	99.5	458	221

Table A2. Trace element contents from ICPMS for 50mg samples (Method 1).

Sample	Seamount	Latitude	Longitude	Sc	Li	V	Cr	Co	Ni	Cu	Zn	Ga	Rb	Sr	Y
NA101-				ppm	ppm	ppm	ppm	ppm	ppm	ppm	ppm	ppm	ppm	ppm	ppm
2	6	26.78962	-166.92227	30.84	17.86	100.44	18.41	6.52	16.76	88.39	126.68	29.32	34.20	943.77	914.30
3	6	26.78985	-166.92056	17.49	18.02	160.13	21.71	23.91	24.77	18.25	125.12	26.43	93.80	915.44	32.07
4	6	26.78933	-166.91755	15.88	16.55	171.01	18.30	25.49	29.31	15.71	106.08	25.48	74.91	907.81	32.13
7	6	26.78856	-166.91240	18.84	20.97	169.30	22.11	23.10	31.65	13.84	83.08	28.47	66.28	1016.87	51.11
8	7	26.78630	-167.35989	27.70	22.61	120.81	36.34	76.36	107.57	64.82	126.15	23.14	54.56	482.93	45.54
10	7	26.78658	-167.36017	31.28	14.80	145.64	14.55	10.26	10.92	43.04	98.01	24.70	69.84	509.91	30.42
12	7	26.79272	-167.36264	18.97	17.89	225.25	80.94	25.04	37.69	54.99	155.94	22.26	28.40	632.00	39.71
15	7	26.80115	-167.36946	35.49	14.49	257.70	130.97	5.59	7.01	25.54	89.04	23.02	68.69	579.26	35.42

21	7	26.80098	-167.37033	40.78	13.47	432.08	129.57	3.11	6.41	19.01	32.40	26.61	30.52	665.08	86.96
23	8	26.85186	-168.06580	11.51	18.03	116.59	9.90	9.97	7.92	16.55	146.82	28.36	33.88	751.64	45.63
24	8	26.85258	-168.06642	11.73	12.24	146.31	9.07	9.08	15.67	25.04	128.36	29.10	66.50	675.96	45.23
26	8	26.85396	-168.06793	11.69	16.93	153.56	16.20	9.81	27.41	38.64	128.42	25.85	34.25	715.20	62.19
30	8	26.85701	-168.07465	16.54	13.42	162.64	12.20	18.19	17.22	21.55	122.96	24.78	54.84	758.60	40.04
33	10	26.97701	-168.85366	24.74	41.43	84.14	173.39	32.91	95.77	47.95	249.48	19.45	34.46	349.82	45.07
39	10	26.97493	-168.85688	24.11	38.65	83.87	186.03	26.76	75.13	47.93	204.03	18.14	34.92	394.68	26.75
43	10	26.97241	-168.86059	24.24	17.79	177.36	109.75	38.77	35.62	10.44	104.18	21.68	34.22	661.96	36.71
44	9	27.03382	-168.49786	15.94	14.20	166.64	0.79	11.57	5.11	9.50	153.09	28.79	40.14	586.47	44.04
45	9	27.03154	-168.49604	18.01	25.65	162.87	2.47	18.21	10.54	21.27	172.87	28.38	33.17	573.23	55.16

49	9	27.02928	-168.49520	22.96	18.68	201.12	16.76	18.36	15.42	38.28	189.78	26.34	31.63	676.77	78.37
51	9	27.02865	-168.49443	14.57	17.05	244.76	3.94	8.11	10.82	27.41	93.30	24.47	57.41	891.84	47.63
56	6	26.70432	-166.98689	14.50	17.75	249.15	2.97	8.92	14.55	35.50	109.42	24.72	84.05	848.84	49.62
58	6	26.70774	-166.98790	14.39	22.12	163.33	2.52	10.46	5.98	18.02	103.02	24.05	49.39	902.92	50.59
68	4	25.97160	-164.74467	24.51	11.76	219.96	124.32	35.26	83.85	23.11	92.94	24.37	49.80	709.07	36.26
71	4	25.97293	-164.74023	22.68	19.88	204.19	126.31	21.09	51.95	58.73	155.64	24.34	46.00	711.90	46.28
74	3	25.55451	-164.20247	16.46	12.85	139.16	11.20	2.85	3.12	14.63	606.66	29.98	26.41	560.31	79.09
75	3	25.55458	-164.20242	20.25	24.82	154.30	2.44	8.65	4.24	16.37	179.83	32.18	14.43	495.70	73.16
88	5	25.72698	-165.42395	14.40	12.24	97.80	0.79	7.72	2.57	14.79	155.56	34.94	69.55	724.43	56.55
94	2	25.40237	-163.92354	25.21	36.54	144.11	70.74	11.72	28.70	47.00	165.57	23.99	40.00	707.69	91.67

97	2	25.40261	-163.92466	21.10	28.94	146.03	69.48	14.05	31.87	39.58	186.03	22.24	92.67	685.43	35.33
99	2	25.40335	-163.92549	23.26	13.99	287.33	63.90	8.65	39.54	57.53	102.29	25.58	46.34	704.24	43.96
102	2	25.40334	-163.92560	37.55	27.23	225.15	45.89	17.40	40.97	51.97	143.50	26.67	65.51	458.50	58.05
104	1	25.32087	-163.74163	26.57	26.35	234.70	85.89	12.53	38.98	56.10	119.17	24.77	29.95	551.90	74.25
106	1	25.32040	-163.74142	29.27	12.68	177.61	102.12	8.76	11.56	12.97	122.20	25.20	59.17	534.76	44.26
113	1	25.31732	-163.74190	36.34	19.53	306.76	47.74	39.16	19.04	62.34	160.79	27.30	33.53	495.00	42.27
114	1	25.31731	-163.74196	35.54	24.11	399.80	9.90	53.35	28.41	81.27	182.73	31.63	41.83	453.83	57.59
Sample	Zr	Nb	Ba	Mo	Cd	Sn	Sb	Cs	La	Ce	Pr	Nd	Sm	Eu	Gd
NA101-	ppm	ppm	ppm	ppm	ppm	ppm	ppm	ppm	ppm	ppm	ppm	ppm	ppm	ppm	ppm
2	243.31	39.27	258.69	0.93	0.13	1.28	3.13	0.98	527.29	66.34	63.47	272.52	46.75	12.72	70.26
3	312.74	64.91	470.50	0.58	0.16	2.13	0.65	2.27	49.32	95.44	11.87	47.65	9.25	2.96	8.30
4	330.76	63.95	465.16	0.38	0.18	2.08	0.57	1.21	48.60	101.05	11.83	46.63	9.00	2.89	8.16
7	323.71	69.99	499.95	0.75	0.14	2.22	0.64	0.56	61.00	101.78	14.22	57.74	11.06	3.49	10.57

8	170.08	39.01	331.53	2.26	0.19	1.39	2.93	1.24	37.44	53.51	8.10	33.20	7.37	2.47	7.91
10	176.28	42.85	356.46	1.01	0.13	1.66	2.38	1.35	29.00	54.86	6.85	28.70	6.49	2.15	6.53
12	166.43	39.08	306.42	1.02	0.13	1.44	1.19	1.25	37.14	52.01	7.20	29.05	6.16	2.12	6.57
15	167.84	37.51	382.14	1.76	0.11	1.54	1.55	1.08	32.29	55.96	7.16	28.91	6.57	2.30	6.88
21	191.71	42.40	379.20	1.20	0.10	1.59	1.79	0.38	64.70	66.67	12.37	52.74	10.94	3.68	12.67
23	370.42	68.94	531.43	0.95	0.16	2.31	0.26	0.24	59.38	121.02	15.22	59.35	11.82	3.62	10.41
24	373.13	80.42	526.31	0.68	0.18	2.29	1.10	0.17	60.22	119.80	15.41	62.82	11.99	3.72	10.75
26	374.12	68.03	494.28	1.46	0.17	7.25	3.16	0.50	65.09	115.97	15.66	61.30	11.85	3.61	11.20
30	271.22	51.44	377.96	2.03	0.14	1.94	0.71	0.90	45.17	92.67	11.81	48.25	9.96	3.20	9.37
33	152.80	28.28	162.51	0.78	0.07	1.09	2.10	1.08	28.40	35.13	5.54	23.64	5.65	1.93	6.81
39	147.55	26.69	153.49	0.71	0.26	1.03	1.93	1.23	16.56	32.64	4.15	17.96	4.66	1.66	5.23
43	183.04	43.82	388.26	0.57	0.13	1.38	0.15	0.07	27.14	54.83	6.87	28.97	7.15	2.55	7.71
44	356.52	63.23	343.50	0.92	0.15	2.36	1.08	0.37	46.12	114.57	12.68	51.49	10.92	3.50	10.49
45	317.94	67.34	324.84	0.63	0.14	64.92	0.84	0.36	58.39	92.13	13.00	54.34	11.10	3.46	10.99
49	320.48	54.95	321.66	1.44	0.17	2.19	0.94	0.66	85.84	93.27	13.16	54.38	10.94	3.43	11.25
51	235.50	59.31	514.92	0.58	0.12	1.65	2.69	0.72	58.25	91.72	12.75	50.85	9.71	3.14	9.56

56	243.61	62.03	518.89	0.43	0.17	1.69	3.23	1.09	57.48	93.34	12.69	50.03	9.73	3.13	9.62
58	234.87	57.74	516.02	0.69	0.12	1.68	1.63	0.89	58.17	88.98	12.90	51.22	9.99	3.17	9.85
68	248.12	50.00	327.06	0.58	0.19	6.41	0.13	0.90	36.39	74.85	9.45	39.43	8.88	2.91	8.55
71	254.06	49.02	322.88	0.83	0.13	2.16	2.79	1.73	44.18	72.35	10.62	44.85	9.63	3.07	9.65
74	388.71	67.32	465.06	1.45	0.16	2.85	0.95	0.18	66.16	104.15	13.85	55.44	11.08	3.80	11.30
75	373.89	69.04	374.24	1.85	0.14	3.00	1.24	0.12	63.23	109.25	14.70	60.99	12.59	3.76	12.58
88	464.64	94.31	518.06	0.85	0.19	3.27	1.12	0.45	70.46	137.25	18.40	77.81	15.68	4.76	14.19
94	196.13	53.91	275.05	0.64	0.09	1.84	1.42	2.03	71.33	69.11	12.52	52.86	10.48	3.27	11.63
97	195.90	49.40	388.94	0.66	0.11	1.65	2.00	5.85	39.55	68.05	8.29	32.67	6.88	2.32	6.74
99	237.80	61.53	456.81	0.93	0.13	1.84	6.55	0.77	42.92	68.14	9.71	39.68	8.34	2.74	8.22
102	408.15	98.38	629.76	2.01	0.20	5.31	1.90	1.07	64.10	120.60	14.13	55.77	11.82	3.55	11.64
104	258.39	39.21	183.91	0.93	0.13	2.16	1.60	1.08	54.45	66.80	13.64	59.62	12.84	3.78	13.67
106	307.18	46.33	269.54	0.87	0.16	2.45	1.25	0.56	37.07	79.73	10.93	47.38	10.41	3.20	10.29
113	283.27	42.26	217.96	1.57	0.12	2.36	0.94	0.81	31.97	67.35	9.28	39.35	9.04	2.92	9.22
114	287.79	53.62	276.48	1.92	0.13	3.30	1.14	1.13	41.10	76.74	11.85	53.68	11.97	3.78	12.23
Sample	Tb	Dy	Ho	Er	Tm	Yb	Lu	Hf	Ta	W	Tl	Pb	Th	U	

NA101-	ppm	ppm	ppm	ppm	ppm	ppm	ppm	ppm	ppm	ppm	ppm	ppm	ppm	ppm	
2	9.68	65.09	15.82	48.72	6.79	42.92	6.70	4.80	2.48	0.52	0.11	8.90	3.61	2.10	
3	1.16	6.20	1.14	2.93	0.40	2.41	0.35	7.16	3.85	0.34	0.21	2.80	5.73	1.37	
4	1.14	6.07	1.11	2.94	0.40	2.42	0.34	7.17	3.92	0.25	0.23	2.74	5.45	1.26	
7	1.48	8.03	1.57	4.08	0.55	3.31	0.50	7.73	4.09	0.40	0.30	3.40	6.01	1.84	
8	1.23	7.41	1.49	4.19	0.59	3.75	0.55	3.90	2.21	0.84	0.63	4.68	3.61	1.98	
10	0.99	5.68	1.10	2.90	0.40	2.46	0.36	4.50	2.39	0.56	0.74	1.81	3.70	2.40	
12	0.97	5.59	1.14	3.09	0.42	2.53	0.37	3.74	2.15	0.19	0.16	2.87	3.20	1.09	
15	1.04	6.08	1.18	3.15	0.43	2.69	0.38	3.97	2.16	1.06	0.14	2.81	3.49	2.40	
21	1.85	11.14	2.26	6.29	0.87	5.37	0.79	4.32	2.39	1.65	0.20	5.45	3.82	1.60	
23	1.49	8.21	1.54	4.15	0.58	3.63	0.52	8.36	4.13	0.37	0.27	3.80	6.97	1.00	
24	1.55	8.40	1.61	4.24	0.59	3.61	0.54	9.34	4.39	0.46	0.17	4.92	7.53	1.04	
26	1.59	9.13	1.82	4.99	0.71	4.55	0.68	8.32	4.19	0.57	0.27	7.08	6.89	1.45	
30	1.35	7.41	1.38	3.68	0.50	3.13	0.46	6.23	3.13	0.31	0.35	2.51	4.80	1.32	
33	1.05	6.29	1.29	3.52	0.49	3.00	0.45	3.80	1.69	0.26	0.10	1.34	2.43	0.69	
39	0.83	4.82	0.92	2.43	0.34	2.03	0.30	3.52	1.55	0.18	0.11	1.28	2.20	0.86	

43	1.19	6.94	1.31	3.43	0.48	2.90	0.41	4.39	2.51	0.19	0.09	1.93	3.41	0.72	
44	1.52	8.52	1.60	4.19	0.57	3.50	0.49	7.92	3.83	0.33	0.16	3.05	4.85	0.99	
45	1.59	8.99	1.80	4.71	0.67	4.11	0.61	7.70	3.67	0.23	0.09	37.28	4.68	1.64	
49	1.60	9.40	1.89	5.17	0.73	4.46	0.68	7.28	3.59	0.22	0.29	4.10	4.37	1.01	
51	1.34	7.69	1.49	3.99	0.56	3.39	0.49	5.08	3.44	0.46	0.21	6.63	5.37	1.28	
56	1.36	7.67	1.52	4.01	0.55	3.43	0.50	5.34	3.63	0.48	0.07	3.24	5.62	1.34	
58	1.40	7.86	1.55	4.15	0.57	3.54	0.51	5.16	3.51	0.36	0.21	6.28	5.60	1.22	
68	1.23	6.90	1.25	3.20	0.43	2.63	0.36	6.03	3.02	0.15	0.05	2.31	3.87	0.82	
71	1.38	7.71	1.47	3.93	0.52	3.21	0.46	6.03	3.16	0.37	0.20	2.57	4.08	1.31	
74	1.60	9.60	2.03	5.76	0.83	5.34	0.80	9.26	4.25	0.98	0.06	5.65	6.96	3.40	
75	1.88	10.80	2.24	6.18	0.90	5.89	0.94	9.04	4.14	0.87	0.15	2.23	7.22	2.47	
88	1.97	10.44	1.96	5.04	0.68	4.15	0.62	11.22	5.58	0.38	0.09	3.48	7.53	1.49	
94	1.68	9.96	2.16	6.01	0.85	5.45	0.87	5.04	3.33	0.29	0.12	2.54	4.63	1.60	
97	0.99	5.66	1.08	2.92	0.41	2.59	0.38	4.65	3.12	0.30	0.07	2.10	4.19	1.31	
99	1.23	6.96	1.38	3.72	0.52	3.25	0.49	5.85	3.55	0.67	0.16	3.96	4.87	1.51	
102	1.70	9.60	1.86	4.96	0.69	4.34	0.64	9.59	6.07	0.40	0.16	4.18	8.24	1.50	

104	1.98	11.64	2.27	6.25	0.85	5.18	0.78	6.23	2.65	0.29	0.78	4.59	3.13	1.50	
106	1.48	8.38	1.59	4.21	0.56	3.46	0.48	7.09	3.04	0.61	0.14	2.59	3.43	1.61	
113	1.35	7.78	1.49	3.90	0.54	3.28	0.47	6.53	2.74	0.26	0.13	1.79	3.13	2.65	
114	1.79	10.11	1.94	4.96	0.67	4.05	0.59	7.98	3.55	0.36	0.38	2.70	4.30	2.60	

Table A3. Trace element contents from ICP-MS for 5mg samples (Method 2).

Sample	NA101-	013	035	043	044	056	063	065	067	070	090	091	093	099	101	102
Seamount		7	10	10	9	6		4	4	4	2	2	2	2	2	2
Latitude		26.79602	26.97599	26.97241	27.03382	26.70432	26.71172	25.97179	25.97186	25.97258	25.39846	25.39848	25.39914	25.40335	25.40339	25.40334
Longitude		-167.36652	-168.85529	-168.86059	-168.49786	-166.98689	-166.98820	-164.74609	-164.74528	-164.74131	-163.91596	-163.91598	-163.91743	-163.92549	-163.92568	-163.92560
Sc	ppm	20.46	22.71	21.74	11.66	11.34	12.49	20.71	17.02	21.80	19.88	21.56	18.95	2.93	19.91	34.77
Li	ppm	16.65	28.22	14.22	12.38	17.18	23.90	8.24	11.61	13.15	9.68	8.30	7.96	14.06	13.67	32.10
V	ppm	270.24	87.61	194.09	154.27	242.84	117.74	201.69	253.99	224.56	230.79	224.33	256.30	254.45	220.54	214.90
Cr	ppm	20.17	211.91	132.55	1.25	1.84	1.89	134.87	82.83	115.70	85.02	91.91	173.15	66.00	94.20	53.92
Co	ppm	7.33	22.27	28.04	10.95	7.58	12.03	19.93	10.29	18.89	19.21	10.32	36.34	4.84	12.09	18.77
Ni	ppm	6.58	64.59	32.59	4.44	16.74	7.95	51.61	48.83	49.46	72.44	49.73	66.48	31.80	57.96	39.24
Cu	ppm	30.57	44.58	5.38	8.62	35.55	32.87	57.74	43.37	61.23	40.99	61.39	53.98	55.97	36.86	42.08
Zn	ppm	155.22	171.88	126.17	134.44	105.12	129.53	123.43	76.16	119.73	94.44	97.90	107.53	89.78	99.54	141.62
Ga	ppm	26.62	18.71	20.56	24.60	22.24	22.28	24.35	23.99	24.47	24.51	23.61	21.64	21.73	22.68	23.39
Rb	ppm	16.14	44.52	35.77	32.79	52.05	33.39	57.80	34.79	44.65	52.22	48.85	68.34	35.73	68.78	91.23

Sr	ppm	768.09	422.52	673.04	546.84	841.99	980.66	714.04	721.15	771.90	622.29	630.00	569.57	694.99	681.24	460.75
Y	ppm	50.70	31.84	37.79	34.79	43.07	55.09	38.41	61.99	97.71	35.52	35.14	42.11	25.36	39.13	52.90
Zr	ppm	217.84	156.30	144.15	328.00	230.20	217.82	267.28	265.09	244.70	250.67	236.56	236.01	236.28	257.85	387.81
Nb	ppm	53.04	28.69	45.29	63.70	64.25	63.07	58.23	59.24	55.26	67.06	64.63	61.67	55.98	69.10	100.53
Mo	ppm	1.47	0.62	0.65	0.97	0.52	0.65	0.73	0.94	1.27	0.90	0.58	0.87	0.82	0.85	1.83
Cd	ppm	0.12	0.14	0.17	0.20	0.18	0.15	0.21	0.19	0.22	0.14	0.12	0.36	0.17	0.21	0.32
Sn	ppm	1.83	1.15	1.15	2.01	1.66	1.53	2.25	2.74	2.21	2.10	2.08	1.90	1.26	2.09	4.73
Sb	ppm	1.62	2.47	0.09	1.10	3.83	1.31	2.52	3.11	5.56	1.21	2.02	4.20	6.87	1.86	1.35
Cs	ppm	0.22	1.53	0.09	0.45	1.09	2.07	0.86	0.61	1.17	0.66	0.68	0.79	0.81	1.53	3.01
Ba	ppm	447.32	223.13	388.89	330.19	487.68	497.40	365.40	376.44	479.00	482.76	461.39	476.72	408.62	473.73	591.30
La	ppm	49.89	19.99	28.59	40.20	49.95	56.22	40.57	50.66	72.24	36.93	36.77	45.96	37.70	45.49	62.62
Ce	ppm	72.80	34.31	53.95	86.57	81.43	85.41	81.14	71.67	85.93	73.38	65.99	72.26	61.00	75.59	117.12
Pr	ppm	10.27	4.71	6.96	11.09	11.26	11.40	10.24	10.54	14.70	8.72	8.83	9.44	8.43	9.77	13.44
Nd	ppm	41.33	20.50	29.87	45.98	45.01	45.51	42.93	44.46	62.07	35.69	36.11	37.91	34.36	39.79	53.05
Sm	ppm	9.23	5.29	7.33	9.76	8.86	8.84	9.56	9.43	13.05	7.76	7.85	7.93	7.16	8.24	11.47
Eu	ppm	3.10	1.92	2.53	3.06	2.81	2.85	3.11	3.07	4.13	2.52	2.57	2.57	2.33	2.71	3.34
Gd	ppm	9.46	6.00	7.96	9.23	8.74	8.83	9.21	9.72	14.02	7.66	7.85	8.13	6.91	8.32	10.72

Tb	ppm	1.47	1.00	1.24	1.40	1.29	1.31	1.38	1.49	2.07	1.14	1.18	1.22	1.05	1.25	1.62
Dy	ppm	8.55	5.81	7.34	7.88	7.43	7.51	7.59	8.58	12.15	6.40	6.69	6.94	6.24	6.99	9.26
Ho	ppm	1.74	1.13	1.40	1.50	1.48	1.56	1.40	1.77	2.49	1.25	1.31	1.37	1.21	1.35	1.78
Er	ppm	4.75	2.89	3.57	3.88	3.86	4.18	3.49	4.65	6.53	3.33	3.47	3.56	3.25	3.49	4.57
Tm	ppm	0.69	0.41	0.50	0.54	0.55	0.62	0.49	0.68	0.94	0.46	0.48	0.52	0.46	0.50	0.66
Yb	ppm	4.31	2.42	3.05	3.23	3.23	3.80	2.84	4.08	5.41	2.78	2.98	3.02	2.86	2.95	4.07
Lu	ppm	0.67	0.36	0.45	0.47	0.49	0.61	0.42	0.64	0.84	0.41	0.43	0.47	0.44	0.44	0.62
Hf	ppm	5.08	3.84	3.87	7.44	5.07	4.75	6.37	6.39	5.84	6.01	5.77	5.48	5.29	6.18	9.65
Ta	ppm	2.86	1.75	2.53	3.63	3.49	3.42	3.34	3.33	3.31	3.72	3.72	3.54	2.95	3.83	6.11
W	ppm	0.52	0.24	0.17	0.38	0.55	0.33	0.34	0.58	0.61	0.42	0.29	0.50	0.58	0.39	0.38
Tl	ppm	0.21	0.14	0.07	0.16	0.09	0.10	0.05	0.08	0.44	0.28	0.08	0.07	0.10	0.07	0.28
Pb	ppm	2.59	1.27	1.62	2.74	2.71	2.78	1.75	2.63	6.60	2.22	2.30	3.41	2.55	2.36	3.05
Th	ppm	4.38	2.74	3.55	3.47	4.38	4.76	4.66	3.82	4.56	4.59	4.07	4.55	2.33	5.17	8.57
U	ppm	1.82	0.65	0.36	0.99	1.27	1.32	1.03	1.47	1.40	1.28	1.38	1.15	1.46	1.32	1.51